

# Chapter 1

## Fiber Gratings

Silica fibers can change their optical properties permanently when they are exposed to intense radiation from a laser operating in the blue or ultraviolet spectral region. This photosensitive effect can be used to induce periodic changes in the refractive index along the fiber length, resulting in the formation of an intracore Bragg grating. Fiber gratings can be designed to operate over a wide range of wavelengths extending from the ultraviolet to the infrared region. The wavelength region near  $1.5 \mu\text{m}$  is of particular interest because of its relevance to fiber-optic communication systems. In this chapter on fiber gratings, the emphasis is on the role of the nonlinear effects. Sections 1.1 and 1.2 discuss the physical mechanism responsible for photosensitivity and various techniques used to make fiber gratings. The coupled-mode theory is described in Section 1.3, where the concept of the photonic bandgap is also introduced. Section 1.4 is devoted to the nonlinear effects occurring under continuous-wave (CW) conditions. The phenomenon of modulation instability is discussed in Section 1.5. The focus of Section 1.6 is on propagation of optical pulses through a fiber grating with emphasis on optical solitons. The phenomenon of nonlinear switching is also covered in this section. Section 1.7 is devoted to related fiber-based periodic structures such as long-period, chirped, sampled, transient, and dynamic gratings together with their applications.

### 1.1 Basic Concepts

Diffraction gratings constitute a standard optical component and are used routinely in various optical instruments such as a spectrometer. The underlying principle was discovered more than 200 years ago [1]. From a practical standpoint, a diffraction grating is defined as any optical element capable of imposing a periodic variation in the amplitude or phase of light incident on it. Clearly, an optical medium whose refractive index varies periodically acts as a grating since it imposes a periodic variation of phase when light propagates through it. Such gratings are called *index gratings*.

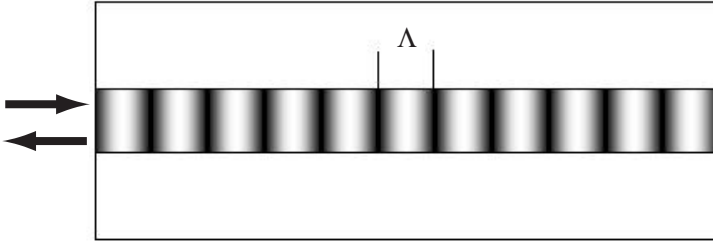


**Figure 1.1:** A fiber grating. Dark and light shaded regions within the fiber core show periodic variations of the refractive index.

### 1.1.1 Bragg Diffraction

The diffraction theory of gratings shows that when light is incident at an angle  $\theta_i$  (measured with respect to the planes of constant refractive index), it is diffracted at an angle  $\theta_r$  such that [1]

$$\sin \theta_i - \sin \theta_r = m\lambda / (\bar{n}\Lambda), \quad (1.1.1)$$

where  $\Lambda$  is the grating period,  $\lambda/\bar{n}$  is the wavelength of light inside the medium with an average refractive index  $\bar{n}$ , and  $m$  is the order of Bragg diffraction. This condition can be thought of as a phase-matching condition, similar to that occurring in the case of Brillouin scattering or four-wave mixing [2] and can be written as

$$\mathbf{k}_i - \mathbf{k}_d = m\mathbf{k}_g, \quad (1.1.2)$$

where  $\mathbf{k}_i$  and  $\mathbf{k}_d$  are the wave vectors associated with the incident and diffracted light. The grating wave vector  $\mathbf{k}_g$  has magnitude  $2\pi/\Lambda$  and points in the direction in which the refractive index of the medium is changing in a periodic manner.

In the case of single-mode fibers, all three vectors lie along the fiber axis. As a result,  $\mathbf{k}_d = -\mathbf{k}_i$  and the diffracted light propagates backward. Thus, as shown schematically in Figure 1.1, a fiber grating acts as a reflector for a specific wavelength of light for which the phase-matching condition is satisfied. In terms of the angles appearing in Eq. (1.1.1),  $\theta_i = \pi/2$  and  $\theta_r = -\pi/2$ . If  $m = 1$ , the period of the grating is related to the vacuum wavelength as  $\lambda = 2\bar{n}\Lambda$ . This condition is known as the *Bragg condition*, and gratings satisfying it are referred to as *Bragg gratings*. Physically, the Bragg condition ensures that weak reflections occurring throughout the grating add up in phase to produce a strong reflection at the input end. For a fiber grating reflecting light in the wavelength region near  $1.5 \mu\text{m}$ , the grating period  $\Lambda \approx 0.5 \mu\text{m}$ .

Bragg gratings inside optical fibers were first formed in 1978 by irradiating a germanium-doped silica fiber for a few minutes with an intense argon-ion laser beam [3]. The grating period was fixed by the argon-ion laser wavelength, and the grating reflected light only within a narrow region around that wavelength. It was realized that the 4% reflection occurring at the two fiber-air interfaces created a standing-wave pattern such that more of the laser light was absorbed in the bright regions. As a result, the glass structure changed in such a way that the refractive index increased permanently in the bright regions. Although this phenomenon attracted some attention during the

next 10 years [4]–[16], it was not until 1989 that fiber gratings became a topic of intense investigation, fueled partly by the observation of second-harmonic generation in photosensitive fibers. The impetus for this resurgence of interest was provided by a 1989 paper in which a side-exposed holographic technique was used to make fiber gratings with controllable period [17].

Because of its relevance to fiber-optic communication systems, the holographic technique was quickly adopted to produce fiber gratings in the wavelength region near  $1.55 \mu\text{m}$  [18]. Considerable work was done during the early 1990s to understand the physical mechanism behind photosensitivity of fibers and to develop techniques that were capable of making large changes in the refractive index [19]–[47]. By 1995, fiber gratings were available commercially, and by 1997 they became a standard component of lightwave technology. Soon after, several books devoted entirely to fiber gratings appeared, focusing on applications related to fiber sensors and fiber-optic communication systems [48]–[50].

### 1.1.2 Photosensitivity

There is considerable evidence that the photosensitivity of optical fibers is due to defect formation inside the core of Ge-doped silica ( $\text{SiO}_2$ ) fibers [29]–[31]. In practice, the core of a silica fiber is often doped with germania ( $\text{GeO}_2$ ) to increase its refractive index and introduce an index step at the core-cladding interface. The Ge concentration is typically 3–5% but may exceed 15% in some cases.

The presence of Ge atoms in the fiber core leads to formation of oxygen-deficient bonds (such as Si–Ge, Si–Si, and Ge–Ge bonds), which act as defects in the silica matrix [48]. The most common defect is the GeO defect. It forms a defect band with an energy gap of about 5 eV (energy required to break the bond). Single-photon absorption of 244-nm radiation from an excimer laser (or two-photon absorption of 488-nm light from an argon-ion laser) breaks these defect bonds and creates  $\text{GeE}'$  centers. Extra electrons associated with  $\text{GeE}'$  centers are free to move within the glass matrix until they are trapped at hole-defect sites to form the color centers known as Ge(1) and Ge(2). Such modifications in the glass structure change the absorption spectrum  $\alpha(\omega)$ . However, changes in the absorption also affect the refractive index since  $\Delta\alpha$  and  $\Delta n$  are related through the Kramers–Kronig relation [51]:

$$\Delta n(\omega') = \frac{c}{\pi} \int_0^\infty \frac{\Delta\alpha(\omega)d\omega}{\omega^2 - \omega'^2}. \quad (1.1.3)$$

Even though absorption modifications occur mainly in the ultraviolet region, the refractive index can change even in the visible or infrared region. Moreover, as index changes occur only in the regions of fiber core where the ultraviolet light is absorbed, a periodic intensity pattern is transformed into an index grating. Typically, index change  $\Delta n$  is  $\sim 10^{-4}$  in the 1.3- to 1.6- $\mu\text{m}$  wavelength range but can exceed 0.001 in fibers with high Ge concentration [34].

The presence of GeO defects is crucial for photosensitivity to occur in optical fibers. However, standard telecommunication fibers rarely have more than 3% of Ge atoms in their core, resulting in relatively small index changes. The use of other

dopants, such as phosphorus, boron, and aluminum, can enhance the photosensitivity (and the amount of index change) to some extent, but these dopants also tend to increase fiber losses. It was discovered in the early 1990s that the amount of index change induced by ultraviolet absorption can be enhanced by two orders of magnitude ( $\Delta n > 0.01$ ) by soaking the fiber in hydrogen gas at high pressures (200 atm) and room temperature [39]. The density of Ge–Si oxygen-deficient bonds increases in hydrogen-soaked fibers because hydrogen can recombine with oxygen atoms. Once hydrogenated, the fiber needs to be stored at low temperature to maintain its photosensitivity. However, gratings made in such fibers remain intact over relatively long periods of time, if they are stabilized using a suitable annealing technique [52]–[56]. Hydrogen soaking is commonly used for making fiber gratings.

Because of the stability issue associated with hydrogen soaking, a technique, known as ultraviolet (UV) hypersensitization, has been employed in recent years [57]–[59]. An alternative method, known as *OH flooding*, is also used for this purpose. In this approach [60], the hydrogen-soaked fiber is heated rapidly to a temperature near 1000°C before it is exposed to UV radiation. The resulting out-gassing of hydrogen creates a flood of OH ions and leads to a considerable increase in the fiber photosensitivity. A comparative study of different techniques revealed that the UV-induced index changes were indeed more stable in the hypersensitized and OH-flooded fibers [61]. It should be stressed that understanding of the exact physical mechanism behind photosensitivity is far from complete, and more than one mechanism may be involved [57]. Localized heating can also affect the formation of a grating. For instance, damage tracks were seen in fibers with a strong grating (index change  $>0.001$ ) when the grating was examined under an optical microscope [34]; these tracks were due to localized heating to several thousand degrees of the core region, where ultraviolet light was most strongly absorbed. At such high temperatures the local structure of amorphous silica can change considerably because of melting.

## 1.2 Fabrication Techniques

Fiber gratings can be made by using several techniques, each having its own merits [48]–[50]. This section discusses briefly four major techniques, used commonly for making fiber gratings: the single-beam internal technique, the dual-beam holographic technique, the phase-mask technique, and the point-by-point fabrication technique. The use of ultrashort optical pulses for grating fabrication is covered in the last subsection.

### 1.2.1 Single-Beam Internal Technique

In this technique, used in the original 1978 experiment [3], a single laser beam, often obtained from an argon-ion laser operating in a single mode near 488 nm, is launched into a germanium-doped silica fiber. The light reflected from the near end of the fiber is then monitored. The reflectivity is initially about 4%, as expected for a fiber–air interface. However, it gradually begins to increase with time and can exceed 90% after a few minutes when the Bragg grating is completely formed [5]. Figure 1.2 shows

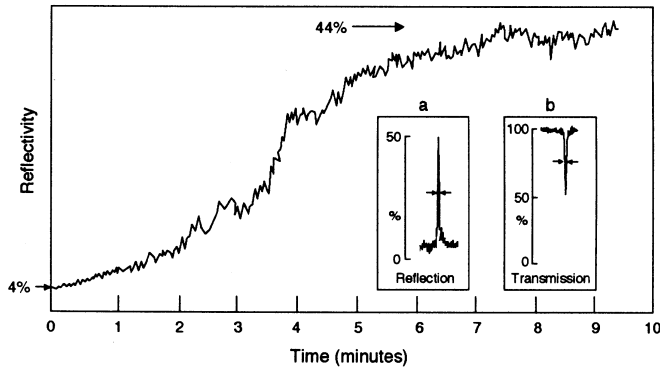


**Figure 1.2:** Increase in reflectivity with time during grating formation. Insets show the reflection and transmission spectra of the grating. (From Ref. [3]; ©1978 AIP.)

the increase in reflectivity with time, observed in the 1978 experiment for a 1-m-long fiber having a numerical aperture of 0.1 and a core diameter of  $2.5 \mu\text{m}$ . Measured reflectivity of 44% after 8 minutes of exposure implies more than 80% reflectivity of the Bragg grating when coupling losses are accounted for.

Grating formation is initiated by the light reflected from the far end of the fiber and propagating in the backward direction. The two counterpropagating waves interfere and create a standing-wave pattern with periodicity  $\lambda/2\bar{n}$ , where  $\lambda$  is the laser wavelength and  $\bar{n}$  is the mode index at that wavelength. The refractive index of silica is modified locally in the regions of high intensity, resulting in a periodic index variation along the fiber length. Even though the index grating is quite weak initially (4% far-end reflectivity), it reinforces itself through a kind of runaway process. Since the grating period is exactly the same as the standing-wave period, the Bragg condition is satisfied for the laser wavelength. As a result, some forward-traveling light is reflected backward through distributed feedback, which strengthens the grating, which in turn increases feedback. The process stops when the photoinduced index change saturates. Optical fibers with an intracore Bragg grating act as a narrowband reflection filter. The two insets in Figure 1.2 show the measured reflection and transmission spectra of such a fiber grating. The full width at half maximum (FWHM) of these spectra is only about 200 MHz.

A disadvantage of the single-beam internal method is that the grating can be used only near the wavelength of the laser used to make it. Since Ge-doped silica fibers exhibit little photosensitivity at wavelengths longer than  $0.5 \mu\text{m}$ , such gratings cannot be used in the 1.3- to  $1.6\text{-}\mu\text{m}$  wavelength region that is important for optical communications. A dual-beam holographic technique, discussed next, solves this problem.

### 1.2.2 Dual-Beam Holographic Technique

The dual-beam holographic technique, shown schematically in Figure 1.3, makes use of an external interferometric scheme similar to that used for holography. Two optical beams, obtained from the same laser (operating in the ultraviolet region) and making

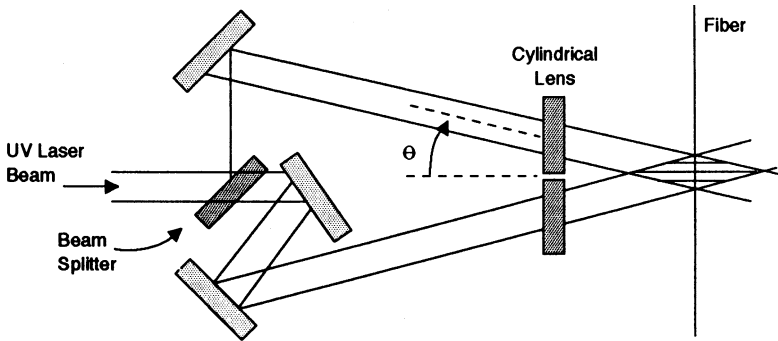


Figure 1.3: The dual-beam holographic technique.

an angle  $2\theta$  are made to interfere at the exposed core of an optical fiber [17]. A cylindrical lens is used to expand the beam along the fiber length. Similar to the single-beam scheme, the interference pattern creates an index grating. However, the grating period  $\Lambda$  is related to the ultraviolet laser wavelength  $\lambda_{\text{uv}}$  and the angle  $2\theta$  made by the two interfering beams through the simple relation

$$\Lambda = \lambda_{\text{uv}} / (2 \sin \theta). \quad (1.2.1)$$

The most important feature of the holographic technique is that the grating period  $\Lambda$  can be varied over a wide range by simply adjusting the angle  $\theta$  (see Figure 1.3). The wavelength  $\lambda$  at which the grating reflects light is related to  $\Lambda$  as  $\lambda = 2\bar{n}\Lambda$ . Since  $\lambda$  can be significantly larger than  $\lambda_{\text{uv}}$ , Bragg gratings operating in the visible or infrared region can be fabricated by the dual-beam holographic method even when  $\lambda_{\text{uv}}$  is in the ultraviolet region. In a 1989 experiment, Bragg gratings reflecting 580-nm light were made by exposing the 4.4-mm-long core region of a photosensitive fiber for 5 minutes with 244-nm ultraviolet radiation [17]. Reflectivity measurements indicated that the refractive index changes were  $\sim 10^{-5}$  in the bright regions of the interference pattern. Bragg gratings formed by the dual-beam holographic technique were stable and remained unchanged even when the fiber was heated to 500°C.

Because of their practical importance, Bragg gratings operating in the 1.55- $\mu\text{m}$  region were made in 1990 [18]. Since then, several variations of the basic technique have been used to make such gratings in a practical manner. An inherent problem for the dual-beam holographic technique is that it requires an ultraviolet laser with excellent temporal and spatial coherence. Excimer lasers commonly used for this purpose have relatively poor beam quality and require special care to maintain the interference pattern over the fiber core over a duration of several minutes.

It turns out that high-reflectivity fiber gratings can be written by using a single excimer laser pulse (with typical duration of 20 ns) if the pulse energy is large enough [32]–[34]. Extensive measurements on gratings made by this technique indicate a thresholdlike phenomenon near a pulse energy level of about 35 mJ [34]. For lower pulse energies, the grating is relatively weak since index changes are only about  $10^{-5}$ . By contrast, index changes of about  $10^{-3}$  are possible for pulse energies above 40 mJ.

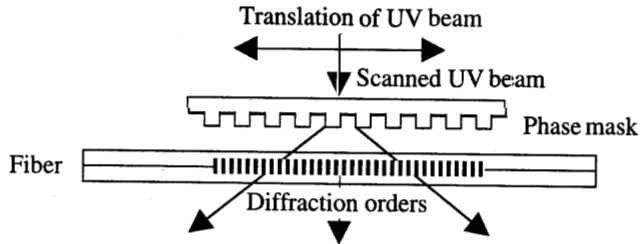


**Figure 1.4:** A phase-mask interferometer used for making fiber gratings. (From Ref. [48]; ©1999 Academic Press.)

Bragg gratings with nearly 100% reflectivity have been made by using a single 40-mJ pulse at the 248-nm wavelength. The gratings remained stable at temperatures as high as 800°C. A short exposure time has an added advantage. The typical rate at which a fiber is drawn from a preform is about 1 m/s. Since the fiber moves only 20 nm in 20 ns and since displacement is a small fraction of the grating period  $\Lambda$ , a grating can be written during the drawing stage, while the fiber is being pulled and before it is sleeved [35]. This feature makes the single-pulse holographic technique quite useful from a practical standpoint.

### 1.2.3 Phase-Mask Technique

This nonholographic technique uses a photolithographic process commonly employed for fabrication of integrated electronic circuits. The basic idea is to use a phase mask with a periodicity related to the grating period [36]. The phase mask acts as a master grating that is transferred to the fiber using a suitable method. In one realization of this technique [37], the phase mask was made on a quartz substrate on which a patterned layer of chromium was deposited using electron-beam lithography in combination with reactive-ion etching. Phase variations induced in the 242-nm radiation passing through the phase mask translate into a periodic intensity pattern similar to that produced by the holographic technique. The photosensitivity of the fiber converts intensity variations into an index grating of the same periodicity as that of the phase mask.

The chief advantage of the phase-mask method is that the demands on the temporal and spatial coherence of the ultraviolet beam are much less stringent because of the noninterferometric nature of the technique. In fact, even a nonlaser source such as an ultraviolet lamp can be used. Furthermore, the phase-mask technique allows fabrication of fiber gratings with a variable period (chirped gratings) and can be used to tailor the periodic index profile along the grating length. It is also possible to vary the Bragg wavelength over some range for a fixed mask periodicity by using a converging or diverging wavefront during the photolithographic process [41]. On the other hand, the quality of fiber grating (length, uniformity, etc.) depends completely on the master phase mask, and all imperfections are reproduced precisely. Nonetheless, gratings with 5-mm length and 94% reflectivity were made in 1993, showing the potential of this technique [37].

The phase mask can be used to form an interferometer using the geometry shown in Figure 1.4. The ultraviolet laser beam falls normally on the phase mask and is diffracted into several beams in the Raman–Nath scattering regime. The zeroth-order beam (direct transmission) is blocked or canceled by an appropriate technique. The two first-order diffracted beams interfere on the fiber surface and form a periodic intensity pattern. The grating period is exactly one half of the phase-mask period. In effect, the phase mask produces both the reference and object beams required for holographic recording.

There are several advantages of using a phase-mask interferometer. It is insensitive to the lateral translation of the incident laser beam and tolerant of any beam-pointing instability. Relatively long fiber gratings can be made by moving two side mirrors while maintaining their mutual separation. In fact, the two mirrors can be replaced by a single silica block that reflects the two beams internally through total internal reflection, resulting in a compact and stable interferometer [48]. The length of the grating formed inside the fiber core is limited by the size and optical quality of the silica block.

Long gratings can be formed by scanning the phase mask or translating the optical fiber itself such that different parts of the optical fiber are exposed to the two interfering beams. In this way, multiple short gratings are formed in succession in the same fiber. Any discontinuity or overlap between the two neighboring gratings, resulting from positional inaccuracies, leads to the so-called stitching errors (also called *phase errors*) that can affect the quality of the whole grating substantially if left uncontrolled. Nevertheless, this technique was used in 1993 to produce a 5-cm-long grating [42]. By 1996, gratings longer than 1 meter have been made with success [62] by employing techniques that minimize phase errors [63].

### 1.2.4 Point-by-Point Fabrication Technique

This nonholographic scanning technique bypasses the need for a master phase mask and fabricates the grating directly on the fiber, period by period, by exposing short sections of width  $w$  to a single high-energy pulse [19]. The fiber is translated by a distance  $\Lambda - w$  before the next pulse arrives, resulting in a periodic index pattern such that only a fraction  $w/\Lambda$  in each period has a higher refractive index. The method is referred to as *point-by-point fabrication* since a grating is fabricated period by period even though the period  $\Lambda$  is typically below  $1\ \mu\text{m}$ . The technique works by focusing the spot size of the ultraviolet laser beam so tightly that only a short section of width  $w$  is exposed to it. Typically,  $w$  is chosen to be  $\Lambda/2$  although it could be a different fraction if so desired.

This technique has a few practical limitations. First, only short fiber gratings ( $<1\ \text{cm}$ ) are typically produced because of the time-consuming nature of the point-to-point fabrication method. Second, it is hard to control the movement of a translation stage accurately enough to make this scheme practical for long gratings. Third, it is not easy to focus the laser beam to a small spot size that is only a fraction of the grating period. Recall that the period of a first-order grating is about  $0.5\ \mu\text{m}$  at  $1.55\ \mu\text{m}$  and becomes even smaller at shorter wavelengths. For this reason, the technique was first demonstrated in 1993 by making a  $360\text{-}\mu\text{m}$ -long, third-order grating with a  $1.59\text{-}\mu\text{m}$

period [38]. The third-order grating still reflected about 70% of the incident 1.55- $\mu\text{m}$  light. From a fundamental standpoint, an optical beam can be focused to a spot size as small as the wavelength. Thus, the 248-nm laser commonly used in grating fabrication should be able to provide a first-order grating in the wavelength range from 1.3 to 1.6  $\mu\text{m}$  with proper focusing optics similar to that used for fabrication of integrated circuits.

The point-by-point fabrication method is quite suitable for long-period gratings in which the grating period exceeds 10  $\mu\text{m}$  and even can be longer than 100  $\mu\text{m}$ , depending on the application [64]–[66]. Such gratings can be used for mode conversion (power transfer from one mode to another) or polarization conversion (power transfer between two orthogonally polarized modes). Their filtering characteristics have been used for flattening the gain profile of erbium-doped fiber amplifiers. Long-period gratings are covered in Section 1.7.1.

### 1.2.5 Technique Based on Ultrashort Optical Pulses

In recent years, femtosecond pulses have been used to change the refractive index of glass locally and to fabricate planar waveguides within a bulk medium [67]–[72]. The same technique can be used for making fiber gratings. Femtosecond pulses from a Ti:sapphire laser operating in the 800-nm regime were used as early as 1999 [73]–[75]. Two distinct mechanisms can lead to index changes when such lasers are used [76]. In the so-called type-I gratings, index changes are of reversible nature. In contrast, permanent index changes occur in type-II gratings because of multiphoton ionization and plasma formation when the peak power of pulses exceeds the self-focusing threshold. The second type of gratings can be written using energetic femtosecond pulses that illuminate an especially made phase mask [74]. They were observed to be stable at temperatures of up to 1000°C in the sense that the magnitude of index change created by the 800-nm femtosecond pulses remained unchanged over hundreds of hours [75].

In an alternative approach, infrared radiation is first converted into the UV region through harmonic generation, before using it for grating fabrication. In this case, photon energy exceeds 4 eV, and the absorption of single photons can create large index changes. As a result, the energy fluence required for forming the grating is reduced considerably [77]–[79]. In practice, one can employ either 264-nm pulses, obtained from fourth harmonic of a femtosecond Nd:glass laser, or 267-nm pulses using third harmonic of a Ti:sapphire laser. In both cases, index changes  $>10^{-3}$  have been realized. Figure 1.5 shows the experimental results obtained when 264-nm pulses of 0.2-nJ energy (pulse width 260 fs) were employed for illuminating a phase mask and forming a 3-mm-long Bragg grating [77]. The left part shows the measured UV-induced change in the refractive index of fiber core as a function of incident energy fluence for (a) a hydrogen-soaked fiber and (b) a hydrogen-free fiber. The transmission spectra of three fiber gratings are shown for fluence values that correspond to the maximum fluence level for the three peak intensities. The topmost spectrum implies a peak reflectivity level of  $>99.9\%$  at the Bragg wavelength and corresponds to a UV-induced change in the refractive index of about  $2 \times 10^{-3}$ . This value was lower for the fiber that was not soaked in hydrogen, but it could be made to exceed  $10^{-3}$  by increasing both the peak-intensity and fluence levels of UV pulses. Similar results were obtained when

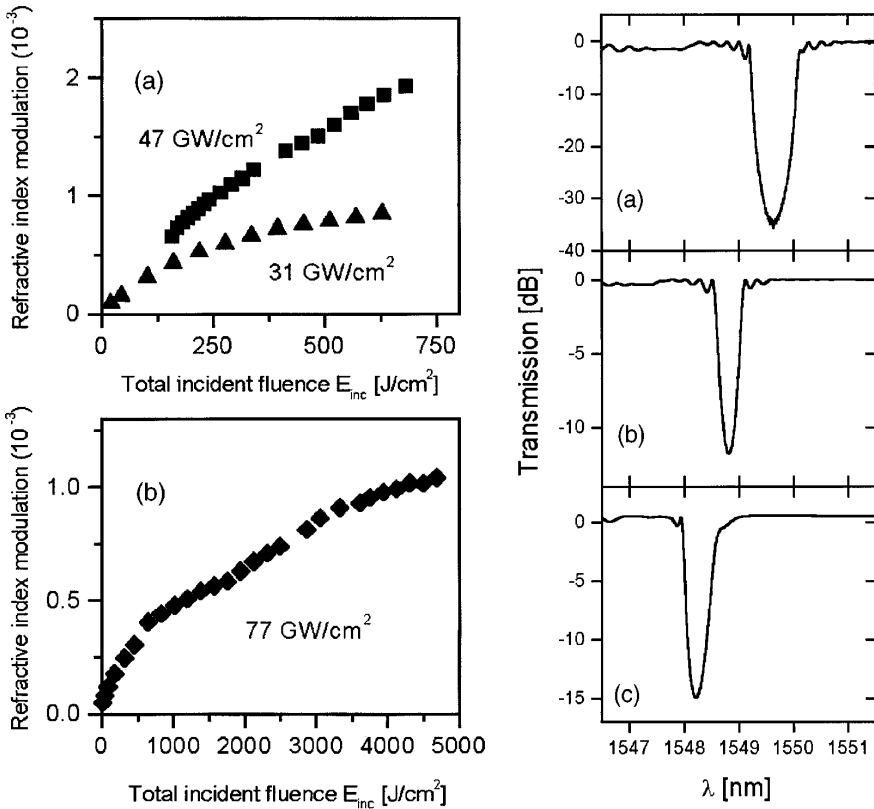


**Figure 1.5:** Left: Index change  $\Delta n$  as a function of incident energy fluence for (a) a hydrogen-soaked fiber and (b) a hydrogen-free fiber. Right: Transmission spectra of three fiber gratings for fluence values that correspond to the maximum fluence level at peak intensities of (a)  $47 \text{ GW/cm}^2$ , (b)  $31 \text{ GW/cm}^2$ , and (c)  $77 \text{ GW/cm}^2$ . (From Ref. [77]; ©2003 OSA.)

267-nm pulses, obtained through third harmonic of a 800-nm Ti:sapphire laser, were employed [78]. Gratings formed with this method are of type-I type in the sense that the magnitude of index change decreases with annealing at high temperatures [79].

### 1.3 Grating Characteristics

Two approaches have been used to study how a Bragg grating affects wave propagation in optical fibers. In one approach, Bloch formalism, used commonly for describing motion of electrons in semiconductors, is applied to Bragg gratings [80]. In another, forward- and backward-propagating waves are treated independently, and the Bragg grating provides a coupling between them. This method, known as the *coupled-mode theory*, has been used with considerable success in several contexts. In this section, we derive the nonlinear coupled-mode equations and use them to discuss propagation

of low-intensity CW light through a Bragg grating. We also introduce the concept of photonic bandgap and use it to show that a Bragg grating introduces a large amount of dispersion.

### 1.3.1 Coupled-Mode Equations

Wave propagation in a linear periodic medium has been studied extensively using coupled-mode theory [81]–[83]. This theory has been applied to distributed-feedback (DFB) semiconductor lasers [84], among other things. In the case of optical fibers, we need to include both the nonlinear nature and the periodic variation of the refractive index by using

$$\tilde{n}(\omega, z) = \bar{n}(\omega) + n_2|E|^2 + \delta n_g(z), \quad (1.3.1)$$

where  $n_2$  is the nonlinear parameter and  $\delta n_g(z)$  accounts for periodic index variations inside the grating. The coupled-mode theory can be generalized to include the fiber nonlinearity since the nonlinear index change  $n_2|E|^2$  in Eq. (1.3.1) is so small that it can be treated as a perturbation [85].

The starting point consists of solving Maxwell's equations with the refractive index given in Eq. (1.3.1). However, as discussed in Section 2.3 of Ref. [2], if the nonlinear effects are relatively weak, we can work in the frequency domain and solve the Helmholtz equation

$$\nabla^2 \tilde{E} + \tilde{n}^2(\omega, z)\omega^2/c^2 \tilde{E} = 0, \quad (1.3.2)$$

where  $\tilde{E}$  denotes the Fourier transform of the electric field with respect to time.

Noting that  $\tilde{n}$  is a periodic function of  $z$ , it is useful to expand  $\delta n_g(z)$  in a Fourier series as

$$\delta n_g(z) = \sum_{m=-\infty}^{\infty} \delta n_m \exp[2\pi i m(z/\Lambda)]. \quad (1.3.3)$$

Since both the forward- and backward-propagating waves should be included,  $\tilde{E}$  in Eq. (1.3.2) is of the form

$$\tilde{E}(\mathbf{r}, \omega) = F(x, y)[\tilde{A}_f(z, \omega) \exp(i\beta_B z) + \tilde{A}_b(z, \omega) \exp(-i\beta_B z)], \quad (1.3.4)$$

where  $\beta_B = \pi/\Lambda$  is the Bragg wave number for a first-order grating. It is related to the Bragg wavelength through the Bragg condition  $\lambda_B = 2\bar{n}\Lambda$  and can be used to define the Bragg frequency as  $\omega_B = \pi c/(\bar{n}\Lambda)$ . Transverse variations for the two counterpropagating waves are governed by the same modal distribution  $F(x, y)$  in a single-mode fiber.

Using Eqs. (1.3.1)–(1.3.4), assuming  $\tilde{A}_f$  and  $\tilde{A}_b$  vary slowly with  $z$  and keeping only the nearly phase-matched terms, the frequency-domain coupled-mode equations become [81]–[83]

$$\frac{\partial \tilde{A}_f}{\partial z} = i[\delta(\omega) + \Delta\beta]\tilde{A}_f + i\kappa\tilde{A}_b, \quad (1.3.5)$$

$$-\frac{\partial \tilde{A}_b}{\partial z} = i[\delta(\omega) + \Delta\beta]\tilde{A}_b + i\kappa\tilde{A}_f, \quad (1.3.6)$$

where  $\delta$ , a measure of detuning from the Bragg frequency, is defined as

$$\delta(\omega) = (\bar{n}/c)(\omega - \omega_B) \equiv \beta(\omega) - \beta_B. \quad (1.3.7)$$

The nonlinear effects in the coupled-mode equations are included through  $\Delta\beta$ . The coupling coefficient  $\kappa$  governs the grating-induced coupling between the forward and backward waves. For a first-order grating,  $\kappa$  is given by

$$\kappa = \frac{k_0 \iint_{-\infty}^{\infty} \delta n_1 |F(x, y)|^2 dx dy}{\iint_{-\infty}^{\infty} |F(x, y)|^2 dx dy}. \quad (1.3.8)$$

In this general form,  $\kappa$  can include transverse variations of  $\delta n_g$  occurring when the photoinduced index change is not uniform over the core area. For a transversely uniform grating  $\kappa = 2\pi\delta n_1/\lambda$ , as can be inferred from Eq. (1.3.8) by taking  $\delta n_1$  as constant and using  $k_0 = 2\pi/\lambda$ . For a sinusoidal grating of the form  $\delta n_g = n_a \cos(2\pi z/\Lambda)$ ,  $\delta n_1 = n_a/2$  and the coupling coefficient is given by  $\kappa = \pi n_a/\lambda$ .

Equations (1.3.5) and (1.3.6) can be converted to time domain by following the procedure outlined in Section 2.3 of Ref. [2]. We assume that the total electric field can be written as

$$E(\mathbf{r}, t) = \frac{1}{2}F(x, y)[A_f(z, t)e^{i\beta_B z} + A_b(z, t)e^{-i\beta_B z}]e^{-i\omega_0 t} + \text{c.c.}, \quad (1.3.9)$$

where  $\omega_0$  is the frequency at which the pulse spectrum is centered. We expand  $\beta(\omega)$  in Eq. (1.3.7) in a Taylor series as

$$\beta(\omega) = \beta_0 + (\omega - \omega_0)\beta_1 + \frac{1}{2}(\omega - \omega_0)^2\beta_2 + \frac{1}{6}(\omega - \omega_0)^3\beta_3 + \dots \quad (1.3.10)$$

and retain terms up to second order in  $\omega - \omega_0$ . The resulting equations are converted into the time domain by replacing  $\omega - \omega_0$  with the differential operator  $i(\partial/\partial t)$ . The resulting time-domain coupled-mode equations have the form

$$\frac{\partial A_f}{\partial z} + \beta_1 \frac{\partial A_f}{\partial t} + \frac{i\beta_2}{2} \frac{\partial^2 A_f}{\partial t^2} + \frac{\alpha}{2} A_f = i\delta A_f + i\kappa A_b + i\gamma(|A_f|^2 + 2|A_b|^2)A_f, \quad (1.3.11)$$

$$-\frac{\partial A_b}{\partial z} + \beta_1 \frac{\partial A_b}{\partial t} + \frac{i\beta_2}{2} \frac{\partial^2 A_b}{\partial t^2} + \frac{\alpha}{2} A_b = i\delta A_b + i\kappa A_f + i\gamma(|A_b|^2 + 2|A_f|^2)A_b, \quad (1.3.12)$$

where  $\delta$  in Eq. (1.3.7) is evaluated at  $\omega = \omega_0$  and becomes  $\delta = (\omega_0 - \omega_B)/v_g$ . In fact, the  $\delta$  term can be eliminated from the coupled-mode equations if  $\omega_0$  is replaced by  $\omega_B$  in Eq. (1.3.9). The other parameters have their traditional meaning. Specifically,  $\beta_1 \equiv 1/v_g$  is related inversely to the group velocity,  $\beta_2$  governs the group-velocity dispersion (GVD), and the nonlinear parameter  $\gamma$  is related to  $n_2$  as  $\gamma = n_2\omega_0/(cA_{\text{eff}})$ , where  $A_{\text{eff}}$  is the effective mode area (see Ref. [2]).

The nonlinear terms in the time-domain coupled-mode equations contain the contributions of both self-phase modulation (SPM) and cross-phase modulation (XPM). In fact, the coupled-mode equations are similar to and should be compared with Eqs. (7.1.15) and (7.1.16) of Ref. [2], which govern the propagation of two copropagating waves inside optical fibers. The two major differences are (i) the negative sign appearing in front of the  $\partial A_b/\partial z$  term in Eq. (1.3.11) because of backward propagation

of  $A_b$  and (ii) the presence of linear coupling between the counterpropagating waves governed by the parameter  $\kappa$ . Both these differences change the character of wave propagation profoundly. Before discussing the general case, it is instructive to consider the case in which the nonlinear effects are so weak that the fiber acts as a linear medium.

### 1.3.2 CW Solution in the Linear Case

In this section, we focus on the linear case in which the nonlinear effects are negligible. When the SPM and XPM terms are neglected in Eqs. (1.3.11) and (1.3.12), the resulting linear equations can be solved easily in the Fourier domain. In fact, we can use Eqs. (1.3.5) and (1.3.6). These frequency-domain coupled-mode equations include GVD to all orders. After setting the nonlinear contribution  $\Delta\beta$  to zero, we obtain

$$\frac{\partial \tilde{A}_f}{\partial z} = i\delta \tilde{A}_f + i\kappa \tilde{A}_b, \quad (1.3.13)$$

$$-\frac{\partial \tilde{A}_b}{\partial z} = i\delta \tilde{A}_b + i\kappa \tilde{A}_f, \quad (1.3.14)$$

where  $\delta(\omega)$  is given in Eq. (1.3.7).

A general solution of these linear equations takes the form

$$\tilde{A}_f(z) = A_1 \exp(iqz) + A_2 \exp(-iqz), \quad (1.3.15)$$

$$\tilde{A}_b(z) = B_1 \exp(iqz) + B_2 \exp(-iqz), \quad (1.3.16)$$

where  $q$  is to be determined. The constants  $A_1$ ,  $A_2$ ,  $B_1$ , and  $B_2$  are interdependent and satisfy the following four relations:

$$(q - \delta)A_1 = \kappa B_1, \quad (q + \delta)B_1 = -\kappa A_1, \quad (1.3.17)$$

$$(q - \delta)B_2 = \kappa A_2, \quad (q + \delta)A_2 = -\kappa B_2. \quad (1.3.18)$$

These equations are satisfied for nonzero values of  $A_1$ ,  $A_2$ ,  $B_1$ , and  $B_2$  if the possible values of  $q$  obey the *dispersion relation*

$$q(\omega) = \pm \sqrt{\delta^2(\omega) - \kappa^2}. \quad (1.3.19)$$

This equation is of paramount importance for gratings. Its implications will become clear soon.

One can eliminate  $A_2$  and  $B_1$  by using Eqs. (1.3.15)–(1.3.18) and write the general solution in terms of an effective reflection coefficient  $r(q)$  as

$$\tilde{A}_f(z) = A_1 \exp(iqz) + r(q)B_2 \exp(-iqz), \quad (1.3.20)$$

$$\tilde{A}_b(z) = B_2 \exp(-iqz) + r(q)A_1 \exp(iqz), \quad (1.3.21)$$

where

$$r(q) = \frac{q - \delta}{\kappa} = -\frac{\kappa}{q + \delta}. \quad (1.3.22)$$

The  $q$  dependence of  $r$  and the dispersion relation (1.3.19) indicate that both the magnitude and the phase of backward reflection depend on the frequency  $\omega$ . The sign ambiguity in Eq. (1.3.19) can be resolved by choosing the sign of  $q$  such that  $|r(q)| < 1$ .

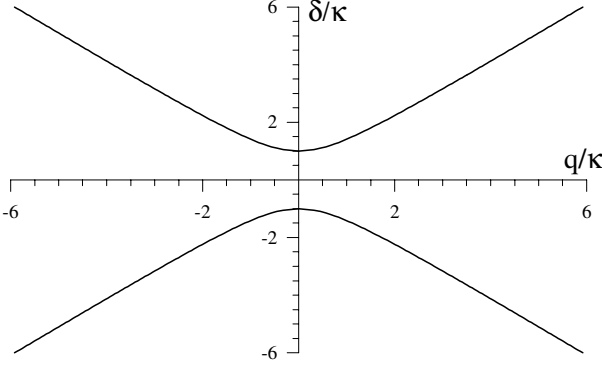


**Figure 1.6:** Dispersion curves showing variation of  $\delta$  with  $q$  and the existence of the photonic bandgap for a fiber grating.

### 1.3.3 Photonic Bandgap

The dispersion relation of Bragg gratings exhibits an important property seen clearly in Figure 1.6, where Eq. (1.3.19) is plotted. If the frequency detuning  $\delta$  of the incident light falls in the range  $-\kappa < \delta < \kappa$ ,  $q$  becomes purely imaginary. Most of the incident field is reflected in that case since the grating does not support a propagating wave. The range  $|\delta| \leq \kappa$  is referred to as the *photonic bandgap*, in analogy with the electronic energy bands occurring in crystals. It is also called the *stop band*, since light stops transmitting through the grating when its frequency falls within the photonic bandgap.

Consider now what happens to an optical pulse propagating inside a fiber grating such that its carrier frequency  $\omega_0$  lies outside the stop band but remains close to a band edge. It follows from Eqs. (1.3.4) and (1.3.15) that the effective propagation constant of the forward-propagating wave is  $\beta_e(\omega) = \beta_B + q(\omega)$ , where  $q(\omega)$  is given by Eq. (1.3.19). The frequency dependence of  $\beta_e$  indicates that a grating exhibits dispersive effects even if it was fabricated in a nondispersive medium. In optical fibers, grating-induced dispersion adds to the material and waveguide dispersions. In fact, the contribution of grating dominates among all sources responsible for dispersion. To see this more clearly, we expand  $\beta_e$  in a Taylor series, in a way similar to Eq. (1.3.10), around the carrier frequency  $\omega_0$  of the pulse. The result is given by

$$\beta_e(\omega) = \beta_0^g + (\omega - \omega_0)\beta_1^g + \frac{1}{2}(\omega - \omega_0)^2\beta_2^g + \frac{1}{6}(\omega - \omega_0)^3\beta_3^g + \dots, \quad (1.3.23)$$

where  $\beta_m^g$  ( $m = 1, 2, \dots$ ) is defined as

$$\beta_m^g = \frac{d^m q}{d\omega^m} \approx \left(\frac{1}{v_g}\right)^m \frac{d^m q}{d\delta^m}, \quad (1.3.24)$$

and the derivatives are evaluated at  $\omega = \omega_0$ . The superscript  $g$  denotes that the dispersive effects have their origin in the grating. In Eq. (1.3.24),  $v_g$  is the group velocity of pulse in the absence of the grating ( $\kappa = 0$ ). It occurs naturally when the frequency

dependence of  $\bar{n}$  is taken into account in Eq. (1.3.7). Dispersion of  $v_g$  is neglected in Eq. (1.3.24) but can be included easily.

Consider first the group velocity of the pulse inside the grating. Using  $V_G = 1/\beta_1^g$  and Eq. (1.3.24), it is given by

$$V_G = \pm v_g \sqrt{1 - \kappa^2/\delta^2}, \quad (1.3.25)$$

where the choice of  $\pm$  signs depends on whether the pulse is moving in the forward or backward direction. Far from the band edges ( $|\delta| \gg \kappa$ ), the optical pulse is unaffected by the grating and travels at the group velocity expected in the absence of the grating. However, as  $|\delta|$  approaches  $\kappa$ , the group velocity decreases and becomes zero at the two edges of the stop band, where  $|\delta| = \kappa$ . Therefore, close to the photonic bandgap, an optical pulse experiences considerable slowing down inside a fiber grating. As an example, its speed is reduced by 50% when  $|\delta|/\kappa \approx 1.18$ .

Second- and third-order dispersive properties of the grating are governed by  $\beta_2^g$  and  $\beta_3^g$ , respectively. Using Eq. (1.3.24) together with the dispersion relation, these parameters are given by

$$\beta_2^g = -\frac{\text{sgn}(\delta)\kappa^2/v_g^2}{(\delta^2 - \kappa^2)^{3/2}}, \quad \beta_3^g = \frac{3|\delta|\kappa^2/v_g^3}{(\delta^2 - \kappa^2)^{5/2}}. \quad (1.3.26)$$

The grating-induced GVD, governed by the parameter  $\beta_2^g$ , depends on the sign of detuning  $\delta$ . Figure 1.7 shows how  $\beta_2^g$  and  $\beta_3^g$  vary with  $\delta$  for three gratings for which  $\kappa$  is in the range of 1 to 10  $\text{cm}^{-1}$ . The GVD is anomalous on the upper branch of the dispersion curve in Figure 1.6, where  $\delta$  is positive and the carrier frequency exceeds the Bragg frequency. In contrast, GVD becomes normal ( $\beta_2^g > 0$ ) on the lower branch of the dispersion curve, where  $\delta$  is negative and the carrier frequency is smaller than the Bragg frequency. The third-order dispersion remains positive on both branches of the dispersion curve. Also note that both  $\beta_2^g$  and  $\beta_3^g$  become infinitely large at the two edges of the stop band.

The dispersive properties of a fiber grating are quite different than those of a uniform fiber. First,  $\beta_2^g$  changes sign on the two sides of the stop band centered at the Bragg wavelength, whose location is easily controlled and can be in any region of the optical spectrum. This is in sharp contrast with the behavior of  $\beta_2$  in standard silica fibers, where  $\beta_2$  changes sign at the zero-dispersion wavelength occurring near 1.3  $\mu\text{m}$ . Second,  $\beta_2^g$  is anomalous on the shorter wavelength side of the stop band, whereas  $\beta_2$  in conventional fibers becomes anomalous for wavelengths longer than the zero-dispersion wavelength. Third, the magnitude of  $\beta_2^g$  exceeds that of  $\beta_2$  by a large factor. Figure 1.7 shows that  $|\beta_2^g|$  can easily exceed  $10^7$   $\text{ps}^2/\text{km}$  for a fiber grating, whereas  $\beta_2$  is  $\sim 10$   $\text{ps}^2/\text{km}$  for standard fibers. This feature can be used for dispersion compensation [86]. Typically, a 10-cm-long grating can compensate the GVD acquired over fiber lengths of 50 km or more. Chirped gratings, discussed in Section 1.7.2, can provide even more dispersion when the wavelength of incident signal falls inside the stop band, although they reflect the dispersion-compensated signal [87].

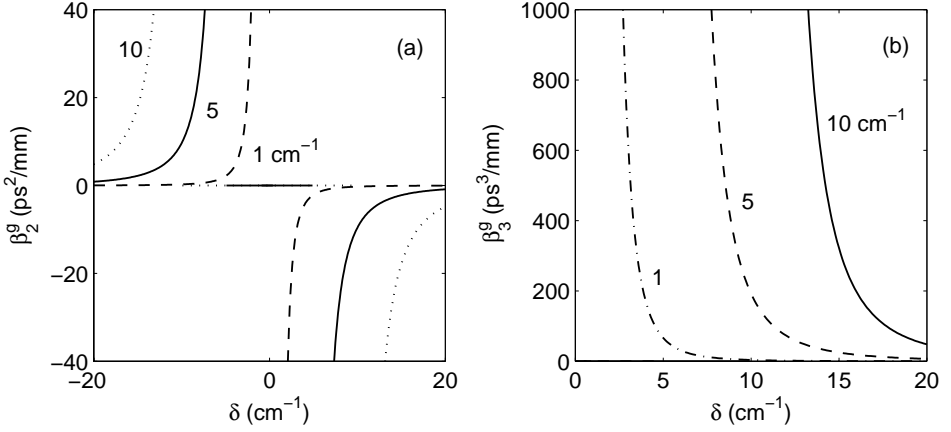


**Figure 1.7:** Second- and third-order dispersion parameters of a fiber grating as a function of detuning  $\delta$  for three values of the coupling coefficient  $\kappa$ .

### 1.3.4 Grating as an Optical Filter

What happens to optical pulses incident on a fiber grating depends very much on the location of the pulse spectrum with respect to the stop band associated with the grating. If the pulse spectrum falls entirely within the stop band, the entire pulse is reflected by the grating. On the other hand, if a part of the pulse spectrum lies outside the stop band, only that part is transmitted through the grating. The shape of the reflected and transmitted pulses in this case becomes quite different than that of the incident pulse because of the splitting of the spectrum and the dispersive properties of the fiber grating. If the peak power of input pulses is small enough that nonlinear effects remain negligible, we can first calculate the reflection and transmission coefficients for each spectral component. The shape of the transmitted and reflected pulses is then obtained by integrating over the spectrum of the incident pulse. Considerable distortion can occur when the pulse spectrum is either wider than the stop band or when it lies in the vicinity of a stop-band edge.

The reflection and transmission coefficients can be calculated by using Eqs. (1.3.20) and (1.3.21) with the appropriate boundary conditions. Consider a grating of length  $L$  and assume that light is incident only at the front end, located at  $z = 0$ . The reflection coefficient is then given by

$$r_g = \frac{\tilde{A}_b(0)}{\tilde{A}_f(0)} = \frac{B_2 + r(q)A_1}{A_1 + r(q)B_2}. \quad (1.3.27)$$

If we use the boundary condition  $\tilde{A}_b(L) = 0$  in Eq. (1.3.21), we find

$$B_2 = -r(q)A_1 \exp(2iqL). \quad (1.3.28)$$

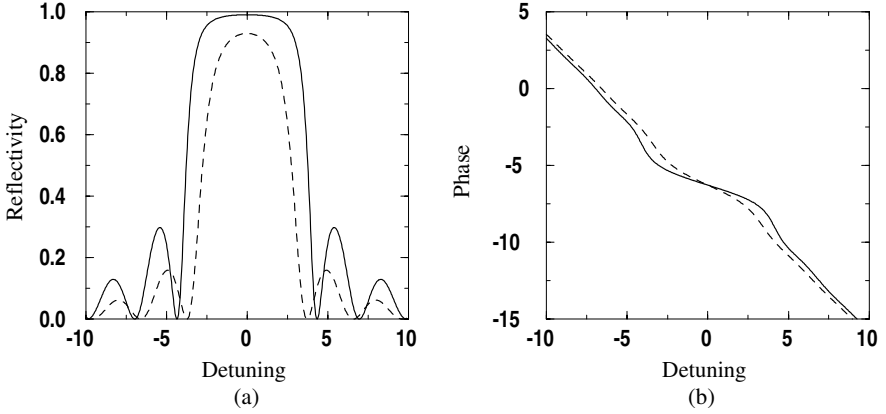


**Figure 1.8:** (a) Reflectivity  $|r_g|^2$  and (b) the phase of  $r_g$  plotted as a function of detuning  $\delta$  for  $\kappa L = 2$  (dashed curves) and  $\kappa L = 3$  (solid curves).

Using  $r(q)$  from Eq. (1.3.22) with this value of  $B_2$  in Eq. (1.3.27), we obtain

$$r_g = \frac{i\kappa \sin(qL)}{q \cos(qL) - i\delta \sin(qL)}. \quad (1.3.29)$$

The transmission coefficient  $t_g$  can be obtained in a similar manner. The frequency dependence of  $r_g$  and  $t_g$  governs the filtering action of a fiber grating.

Figure 1.8 shows the reflectivity  $|r_g|^2$  and the phase of  $r_g$  as a function of detuning  $\delta$  for two values of  $\kappa L$ . The grating reflectivity within the stop band approaches 100% for  $\kappa L = 3$  or larger. Maximum reflectivity occurs at the center of the stop band and, by setting  $\delta = 0$  in Eq. (1.3.29), is given by

$$R_{\max} = |r_g|^2 = \tanh^2(\kappa L). \quad (1.3.30)$$

For  $\kappa L = 2$ ,  $R_{\max} = 0.93$ . The condition  $\kappa L > 2$  with  $\kappa = 2\pi\delta n_1/\lambda$  can be used to estimate the grating length required for high reflectivity inside the stop band. For  $\delta n_1 \approx 10^{-4}$  and  $\lambda = 1.55 \mu\text{m}$ ,  $L$  should exceed 5 mm to yield  $\kappa L > 2$ . These requirements are easily met in practice. Indeed, reflectivities in excess of 99% were achieved for a grating length of 1.5 cm [34].

### 1.3.5 Experimental Verification

The coupled-mode theory has been quite successful in explaining the observed features of fiber gratings. As an example, Figure 1.9 shows the measured reflectivity spectrum for a Bragg grating operating near  $1.3 \mu\text{m}$  [33]. The fitted curve was calculated using Eq. (1.3.29). The 94% peak reflectivity indicates  $\kappa L \approx 2$  for this grating. The stop band is about 1.7-nm wide. These measured values were used to deduce a grating length of 0.84 mm and an index change of  $1.2 \times 10^{-3}$ . The coupled-mode theory explains the observed reflection and transmission spectra of fiber gratings quite well.

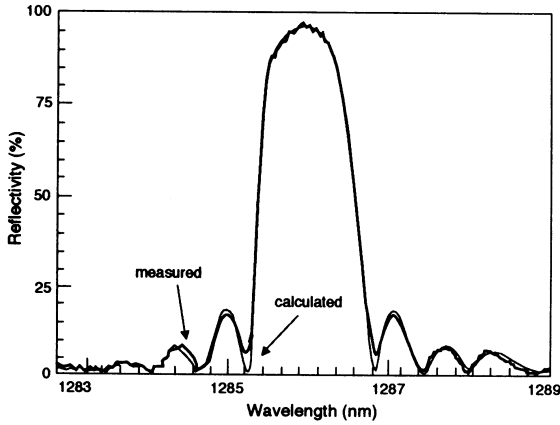


**Figure 1.9:** Measured and calculated reflectivity spectra for a fiber grating operating at wavelengths near  $1.3 \mu\text{m}$ . (From Ref. [33]); ©1993 IEE.)

From a practical standpoint, an undesirable feature seen in Figures 1.8 and 1.9 is the presence of multiple sidebands located on each side of the stop band. These sidebands originate from weak reflections occurring at the two grating ends where the refractive index changes suddenly compared to its value outside the grating region. Even though the change in refractive index is typically less than 1%, the reflections at the two grating ends form a Fabry–Perot cavity with its own wavelength-dependent transmission. An *apodization technique* is commonly used to remove the sidebands seen in Figures 1.8 and 1.9 [48]. In this technique, the intensity of the ultraviolet laser beam used to form the grating is made nonuniform in such a way that the intensity drops to zero gradually near the two grating ends.

Figure 1.10(a) shows schematically how the refractive index varies along the length of an apodized fiber grating. In a transition region of width  $L_t$  near the grating ends, the value of the coupling coefficient  $\kappa$  increases from zero to its maximum value. These buffer zones can suppress the sidebands almost completely, resulting in fiber gratings with practically useful filter characteristics. Figure 1.10(b) shows the measured reflectivity spectrum of a 7.5-cm-long apodized fiber grating, made with the scanning phase-mask technique. The reflectivity exceeds 90% within the stop band, about 0.17-nm wide and centered at the Bragg wavelength of  $1.053 \mu\text{m}$ , chosen to coincide with the wavelength of an Nd:YLF laser [88]. From the stop-band width, the coupling coefficient  $\kappa$  is estimated to be about  $7 \text{ cm}^{-1}$ . Note the sharp drop in reflectivity at both edges of the stop band and a complete absence of sidebands.

The same apodized fiber grating was used to investigate the dispersive properties in the vicinity of a stop-band edge by transmitting 80-ps pulses (with a nearly Gaussian shape) through it [88]. Figure 1.11 shows changes in (a) the pulse width and (b) the transit time during pulse transmission as a function of the detuning  $\delta$  from the Bragg wavelength. For positive values of  $\delta$ , grating-induced GVD is anomalous on the upper branch of the dispersion curve. The most interesting feature is the increase in the arrival time observed as the laser is tuned close to the stop-band edge because of a

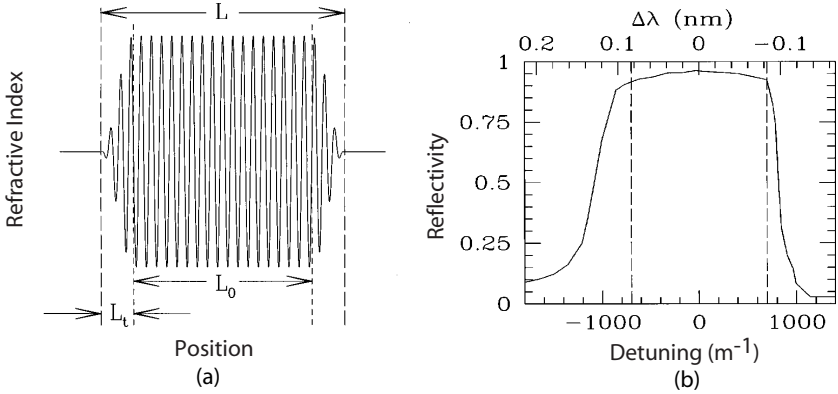


**Figure 1.10:** (a) Schematic variation of refractive index and (b) measured reflectivity spectrum for an apodized fiber grating. (From Ref. [88]; ©1999 OSA.)

reduced group velocity. Doubling of the arrival time for  $\delta$  close to  $900 \text{ m}^{-1}$  shows that the pulse speed was only 50% of that expected in the absence of the grating. This result is in agreement with the prediction of coupled-mode theory in Eq. (1.3.25).

Changes in the pulse width seen in Figure 1.11 can be attributed mostly to the grating-induced GVD effects governed by Eq. (1.3.26). The large broadening observed near the stop-band edge is due to an increase in  $|\beta_2^g|$ . Slight compression near  $\delta = 1200 \text{ m}^{-1}$  is due to a small amount of SPM that chirps the pulse. Indeed, it was necessary to include the  $\gamma$  term in Eqs. (1.3.11) and (1.3.12) to fit the experimental data. The nonlinear effects became quite significant at high power levels. We turn to this issue next.

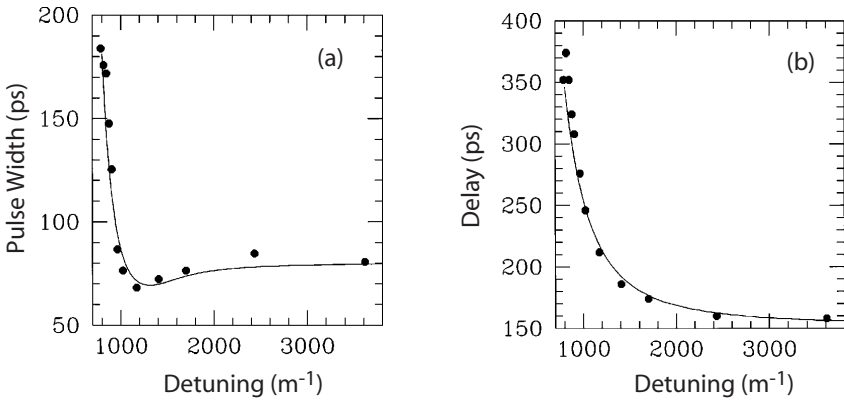


**Figure 1.11:** (a) Measured pulse width (FWHM) of 80-ps input pulses and (b) their arrival time as a function of detuning  $\delta$  for an apodized 7.5-cm-long fiber grating. Solid lines show the prediction of the coupled-mode theory. (From Ref. [88]; ©1999 OSA.)

## 1.4 CW Nonlinear Effects

Wave propagation in a nonlinear, one-dimensional, periodic medium has been studied in several contexts [89]–[109]. In the case of a fiber grating, the presence of an intensity-dependent term in Eq. (1.3.1) leads to SPM and XPM of counterpropagating waves. These nonlinear effects can be included by solving the nonlinear coupled-mode equations, Eqs. (1.3.11) and (1.3.12). In this section, these equations are used to study the nonlinear effects for CW beams. The time-dependent effects are discussed in later sections.

### 1.4.1 Nonlinear Dispersion Curves

In almost all cases of practical interest, the  $\beta_2$  term can be neglected in Eqs. (1.3.11) and (1.3.12). For typical grating lengths ( $<1$  m), the loss term can also be neglected by setting  $\alpha = 0$ . The nonlinear coupled-mode equations then take the following form:

$$i \frac{\partial A_f}{\partial z} + \frac{i}{v_g} \frac{\partial A_f}{\partial t} + \delta A_f + \kappa A_b + \gamma(|A_f|^2 + 2|A_b|^2)A_f = 0, \quad (1.4.1)$$

$$-i \frac{\partial A_b}{\partial z} + \frac{i}{v_g} \frac{\partial A_b}{\partial t} + \delta A_b + \kappa A_f + \gamma(|A_b|^2 + 2|A_f|^2)A_b = 0, \quad (1.4.2)$$

where  $v_g = 1/\beta_1$  and is the group velocity far from the stop band of the grating. These equations exhibit many interesting nonlinear effects. We begin by considering the CW solution of Eqs. (1.4.1) and (1.4.2) imposing no boundary conditions. Even though this is unrealistic from a practical standpoint, the resulting dispersion curves provide considerable physical insight. Note that all grating-induced dispersive effects are included in these equations through the  $\kappa$  term.

To solve Eqs. (1.4.1) and (1.4.2) in the CW limit, we neglect the time-derivative term and assume the following form for the solution:

$$A_f = u_f \exp(iqz), \quad A_b = u_b \exp(iqz), \quad (1.4.3)$$

where  $u_f$  and  $u_b$  remain constant along the grating length. By introducing a parameter  $f = u_b/u_f$  that describes how the total power  $P_0 = u_f^2 + u_b^2$  is divided between the forward- and backward-propagating waves,  $u_f$  and  $u_b$  can be written as

$$u_f = \sqrt{\frac{P_0}{1+f^2}}, \quad u_b = \sqrt{\frac{P_0}{1+f^2}} f. \quad (1.4.4)$$

The parameter  $f$  can be positive or negative. For values of  $|f| > 1$ , the backward wave dominates. By using Eqs. (1.4.1)–(1.4.4),  $q$  and  $\delta$  are found to depend on  $f$  as

$$q = -\frac{\kappa(1-f^2)}{2f} - \frac{\gamma P_0}{2} \frac{1-f^2}{1+f^2}, \quad \delta = -\frac{\kappa(1+f^2)}{2f} - \frac{3\gamma P_0}{2}. \quad (1.4.5)$$

To understand the physical meaning of Eq. (1.4.5), let us first consider the low-power case so that nonlinear effects are negligible. If we set  $\gamma = 0$  in Eq. (1.4.5),

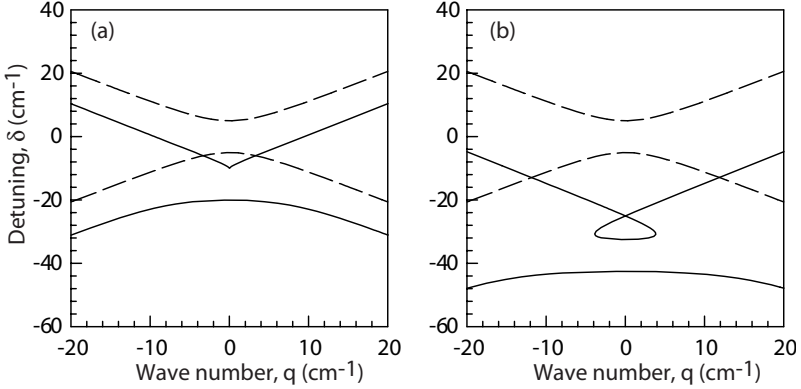


**Figure 1.12:** Nonlinear dispersion curves showing variation of  $\delta$  with  $q$  for (a)  $\gamma P_0/\kappa = 2$  and (b)  $\gamma P_0/\kappa = 5$ , when  $\kappa = 5 \text{ cm}^{-1}$ . Dashed curves show the linear case ( $\gamma = 0$ ).

it is easy to show that  $q^2 = \delta^2 - \kappa^2$ . This is precisely the dispersion relation (1.3.19) obtained previously. As  $f$  changes,  $q$  and  $\delta$  trace the dispersion curves shown in Figure 1.6. In fact,  $f < 0$  on the upper branch while positive values of  $f$  belong to the lower branch. The two edges of the stop band occur at  $f = \pm 1$ . From a practical standpoint, the detuning  $\delta$  of the CW beam from the Bragg frequency determines the value of  $f$ , which in turn fixes the values of  $q$  from Eq. (1.4.5). The group velocity inside the grating also depends on  $f$  and is given by

$$V_G = v_g \frac{d\delta}{dq} = v_g \left( \frac{1 - f^2}{1 + f^2} \right). \quad (1.4.6)$$

As expected,  $V_G$  becomes zero at the edges of the stop band corresponding to  $f = \pm 1$ . Note that  $V_G$  becomes negative for  $|f| > 1$ . This is not surprising if we note that the backward-propagating wave is more intense in that case. The speed of light is reduced considerably as the CW-beam frequency approaches an edge of the stop band. As an example, it reduces by 50% when  $f^2$  equals 1/3 or 3.

Equation (1.4.5) can be used to find how the dispersion curves are affected by the fiber nonlinearity. Figure 1.12 shows such curves at two power levels. The nonlinear effects change the upper branch of the dispersion curve qualitatively, leading to the formation a loop beyond a critical power level. This critical value of  $P_0$  can be found by looking for the value of  $f$  at which  $q$  becomes zero while  $|f| \neq 1$ . From Eq. (1.4.5), we find that this can occur when

$$f \equiv f_c = -(\gamma P_0/2\kappa) + \sqrt{(\gamma P_0/2\kappa)^2 - 1}. \quad (1.4.7)$$

Therefore, a loop is formed only on the upper branch, where  $f < 0$ . Moreover, it can form only when the total power  $P_0 > P_c$ , where  $P_c = 2\kappa/\gamma$ . Physically, an increase in the mode index through the nonlinear term in Eq. (1.3.1) increases the Bragg wavelength and shifts the stop band toward lower frequencies. Since the amount of shift depends on the total power  $P_0$ , light at a frequency close to the edge of the upper

branch can be shifted out of resonance with changes in its power. If the nonlinear parameter  $\gamma$  were negative (self-defocusing medium with  $n_2 < 0$ ), the loop will form on the lower branch in Figure 1.12, as is also evident from Eq. (1.4.7).

## 1.4.2 Optical Bistability

The simple CW solution given in Eq. (1.4.3) is modified considerably when boundary conditions are introduced at the two grating ends. For a finite-size grating, the simplest manifestation of the nonlinear effects occurs through optical bistability, first predicted in 1979 [89].

Consider a CW beam incident at one end of the grating and ask how the fiber nonlinearity would affect its transmission through the grating. It is clear that both the beam intensity and its wavelength with respect to the stop band plays an important role. Mathematically, we should solve Eqs. (1.4.1) and (1.4.2) after imposing the appropriate boundary conditions at  $z = 0$  and  $z = L$ . These equations are similar to those found in Section 6.3 of Ref. [2] and can be solved in terms of the elliptic functions by using the same technique used there [89]. Using  $A_j = \sqrt{P_j} \exp(i\phi_j)$  and separating the real and imaginary parts, Eqs. (1.4.1) and (1.4.2) lead to the following three equations:

$$\frac{dP_f}{dz} = 2\kappa\sqrt{P_f P_b} \sin \psi, \quad (1.4.8)$$

$$\frac{dP_b}{dz} = 2\kappa\sqrt{P_f P_b} \sin \psi, \quad (1.4.9)$$

$$\frac{d\psi}{dz} = 2\delta + 3\gamma(P_f + P_b) + \frac{P_f + P_b}{(P_f P_b)^{1/2}} \kappa \cos \psi, \quad (1.4.10)$$

where  $\psi$  represents the phase difference  $\phi_f - \phi_b$ .

It turns out that the preceding equations have the following two constants of motion [104]:

$$P_f(z) - P_b(z) = P_t, \quad \sqrt{P_f P_b} \cos \psi + (2\delta + 3\gamma P_b)P_f / (2\kappa) = \Gamma_0, \quad (1.4.11)$$

where  $P_t$  is the transmitted power and  $\Gamma_0$  is a constant. Using them, we can derive a differential equation for  $P_f$  that can be solved in terms of the elliptic functions. The use of the boundary condition  $P_b(0) = 0$  then allows us to obtain an implicit relation for the transmitted power  $P_t$  at  $z = L$  as a function of the incident power  $P_i$  for a grating of finite length  $L$ . The reader should consult Ref. [101] for further details.

Figure 1.13 shows the transmitted versus incident power, both normalized to a critical power  $P_{cr} = 4/(3\gamma L)$ , for several values of detuning within the stop band by taking  $\kappa L = 2$ . The S-shaped curves are well known in the context of optical bistability occurring when a nonlinear medium is placed inside a cavity [110]. In fact, the middle branch of these curves with negative slope is unstable, and the transmitted power exhibits hysteresis, as indicated by the arrows on the solid curve. At low powers, transmittivity is small, as expected from the linear theory since the nonlinear effects are relatively weak. However, above a certain input power, most of the incident power is transmitted. Switching from a low-to-high transmission state can be understood qualitatively by noting that the effective detuning  $\delta$  in Eqs. (1.4.1) and (1.4.2) becomes

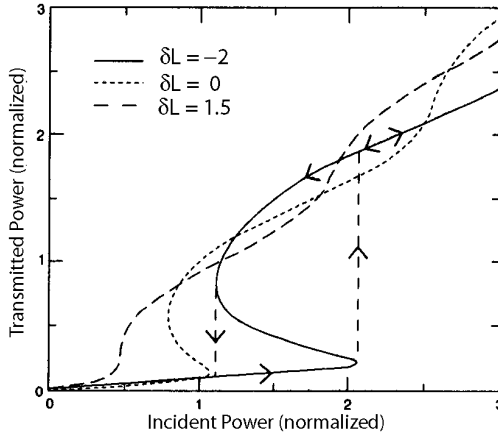


**Figure 1.13:** Transmitted versus incident powers for three values of detuning within the stop band. (From Ref. [89]; ©1979 AIP.)

power dependent because of the nonlinear contribution to the refractive index in Eq. (1.3.1). Thus, light that is mostly reflected at low powers, because its wavelength is inside the stop band, may tune itself out of the stop band and get transmitted when the nonlinear index change becomes large enough.

The observation of optical bistability in fiber gratings is hampered by the large switching power required ( $P_0 > P_{cr} > 1$  kW). It turns out that the switching power can be reduced by a factor of 100 or more by introducing a  $\pi/2$  phase shift in the middle of the fiber grating. Such gratings are called  $\lambda/4$ -shifted or phase-shifted gratings since a distance of  $\lambda/4$  (half grating period) corresponds to a  $\pi/2$  phase shift. They are used routinely for making DFB semiconductor lasers [84]. Their use for fiber gratings was suggested in 1994 [111]. The  $\pi/2$  phase shift opens a narrow transmission window within the stop band of the grating. Figure 1.14(a) compares the transmission spectra for the uniform and phase-shifted gratings at low powers. At high powers, the central peak bends to the left, as seen in the traces in Figure 1.14(b). This bending leads to low-threshold optical switching in phase-shifted fiber gratings [104]. The elliptic-function solution of uniform gratings can be used to construct the multivalued solution for a  $\lambda/4$ -shifted grating [105]. The presence of a phase-shifted region lowers the switching power considerably.

The bistable switching does not always lead to a constant output power when a CW beam is transmitted through a grating. As early as 1982, numerical solutions of Eqs. (1.4.1) and (1.4.2) showed that transmitted power can become not only periodic but also chaotic under certain conditions [90]. In physical terms, portions of the upper branch in Figure 1.13 become unstable under certain conditions. As a result, the output becomes periodic or chaotic once the beam intensity exceeds the switching threshold. This behavior has been observed experimentally and is discussed in Section 1.6. In the following section, we turn to another instability that occurs even when the CW beam is tuned outside the stop band and does not exhibit optical bistability.

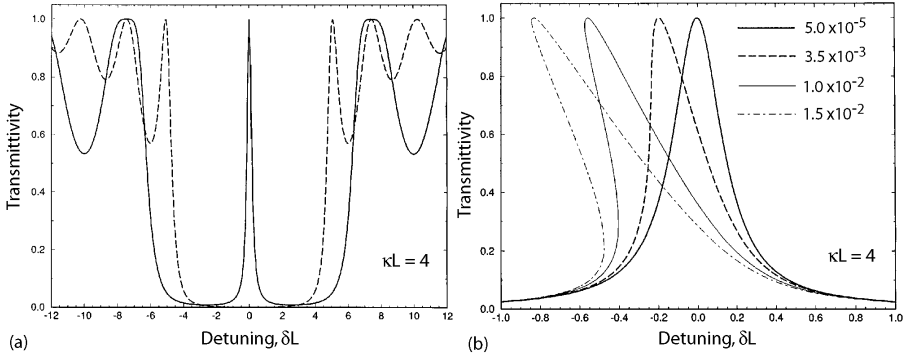


**Figure 1.14:** (a) Transmission spectrum of a fiber grating with (solid curve) and without (dashed curve) a  $\pi/2$  phase shift. (b) Bending of the central transmission peak with increasing input power normalized to the critical power. (From Ref. [104]; ©1995 OSA.)

## 1.5 Modulation Instability

The stability issue is of paramount importance and must be addressed for the CW solutions obtained in the previous section. Similar to the situation discussed in Section 5.1 of Ref. [2], modulation instability can destabilize the steady-state solution and produce periodic output, even when a CW beam is incident on one end of the fiber grating [112]–[118]. Moreover, the repetition rate of pulse trains generated through modulation instability can be tuned over a large range because of large GVD changes occurring with the detuning  $\delta$ .

### 1.5.1 Linear Stability Analysis

For simplicity, we discuss modulation instability using the CW solution given in Eqs. (1.4.3) and (1.4.4) and obtained without imposing the boundary conditions at the grating ends. Following the usual approach [2], we perturb the steady state slightly as

$$A_f = (u_f + a_f)e^{iqz}, \quad A_b = (u_b + a_b)e^{iqz}, \quad (1.5.1)$$

and linearize Eqs. (1.4.1) and (1.4.2), assuming that the perturbations  $a_f$  and  $a_b$  are small. The resulting equations are [117]

$$i \frac{\partial a_f}{\partial z} + \frac{i}{v_g} \frac{\partial a_f}{\partial t} + \kappa a_b - \kappa f a_f + \Gamma[(a_f + a_f^*) + 2f(a_b + a_b^*)] = 0, \quad (1.5.2)$$

$$-i \frac{\partial a_b}{\partial z} + \frac{i}{v_g} \frac{\partial a_b}{\partial t} + \kappa a_f - \frac{\kappa}{f} a_b + \Gamma[2f(a_f + a_f^*) + f^2(a_b + a_b^*)] = 0, \quad (1.5.3)$$

where  $\Gamma = \gamma P_0 / (1 + f^2)$  is an effective nonlinear parameter.

The preceding set of two linear coupled equations can be solved by assuming a plane-wave solution of the form

$$a_j = c_j \exp[i(Kz - \Omega t)] + d_j \exp[-i(Kz + \Omega t)], \quad (1.5.4)$$

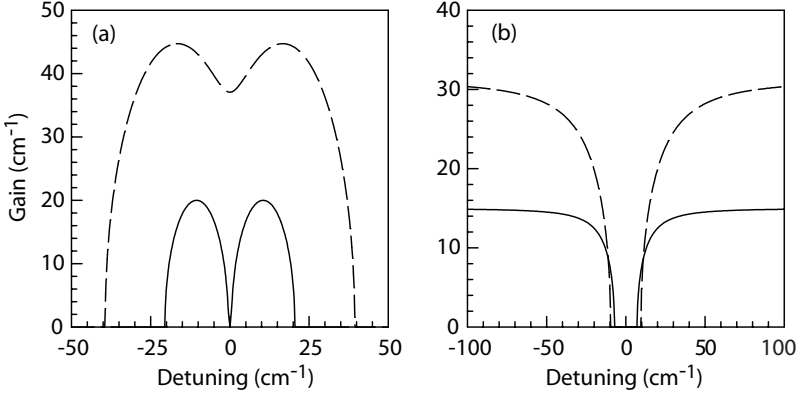


**Figure 1.15:** Gain spectra of modulation instability in the (a) anomalous- and (b) normal-GVD regions of a fiber grating ( $f = \pm 0.5$ ) at two power levels corresponding to  $\Gamma/\kappa = 0.5$  and 2.

where the subscript  $j = f$  or  $b$ . From Eqs. (1.5.2)–(1.5.4), we obtain a set of four homogeneous equations satisfied by  $c_j$  and  $d_j$ . This set has a nontrivial solution only when the  $4 \times 4$  determinant formed by the coefficients matrix vanishes. This condition leads to the the following fourth-order polynomial:

$$(s^2 - K^2)^2 - 2\kappa^2(s^2 - K^2) - \kappa^2 f^2 (s + K)^2 - \kappa^2 f^{-2} (s - K)^2 - 4\kappa\Gamma f (s^2 - 3K^2) = 0, \quad (1.5.5)$$

where we have introduced a spatial frequency as  $s = \Omega/v_g$ .

The four roots of the polynomial in Eq. (1.5.5) determine the stability of the CW solution. However, a tricky issue must be resolved first. Equation (1.5.5) is a fourth-order polynomial in both  $s$  and  $K$ . The question is, which one determines the gain associated with modulation instability? In the case of the uniform-index fibers discussed in Section 5.1 of Ref. [2], the gain  $g$  is related to the imaginary part of  $K$  as light propagates only in the forward direction. In a fiber grating, light travels both forward and backward simultaneously, and it is time that moves forward for both of them. As a result, Eq. (1.5.5) should be viewed as a fourth-order polynomial in  $s$  whose roots depend on  $K$ . The gain of modulation instability is obtained using  $g = 2\text{Im}(s_m)$ , where  $s_m$  is the root with the largest imaginary part.

The root analysis of the polynomial in Eq. (1.5.5) leads to several interesting conclusions [117]. Figure 1.15 shows the gain spectra of modulation instability in the anomalous- and normal-GVD regions, corresponding to upper and lower branches of the dispersion curves, for two values of  $\Gamma/\kappa$ . In the anomalous-GVD case and at relatively low powers ( $\Gamma < \kappa$ ), the gain spectrum is similar to that found for uniform-index fibers. As shown later in this section, the nonlinear coupled-mode equations reduce to a nonlinear Schrödinger (NLS) equation when  $\Gamma \ll \kappa$ . At high values of  $P_0$  such that  $\Gamma > \kappa$ , the gain exists even at  $s = 0$ , as seen in Figure 1.15(a) for  $\Gamma/\kappa = 2$ . Thus, the CW solution becomes unstable at high power levels even to zero-frequency (dc) fluctuations.

Modulation instability can occur even on the lower branch of the dispersion curve ( $f > 0$ ), where grating-induced GVD is normal. The instability occurs only when  $P_0$  exceeds a certain value such that

$$P_0 > \frac{1}{2} \kappa (1 + f^2)^2 f^p, \quad (1.5.6)$$

where  $p = 1$  if  $f \leq 1$  but  $p = -3$  when  $f > 1$ . The occurrence of modulation instability in the normal-GVD region is solely a grating-induced feature.

The preceding analysis completely ignores boundary conditions. For a finite-length grating, one should examine the stability of the CW solution obtained in terms of the elliptic functions. Such a study is complicated and requires a numerical solution to the nonlinear coupled-mode equations [113]. The results show that portions of the upper branch of the bistability curves in Figure 1.13 can become unstable, resulting in the formation of a pulse train through modulation instability. The resulting pulse train is not necessarily periodic and, under certain conditions, can exhibit period doubling and optical chaos.

## 1.5.2 Effective NLS Equation

The similarity of the gain spectrum in Figure 1.15 with that occurring in uniform-index fibers indicates that, at not-too-high power levels, the nonlinear coupled-mode equations predict features that coincide with those found for the NLS equation. Indeed, under certain conditions, Eqs. (1.4.3) and (1.4.4) can be reduced formally to an effective NLS equation [119]–[123]. A multiple-scale method is commonly used to prove this equivalence; details can be found in Ref. [101].

The analysis used to reduce the nonlinear coupled-mode equations to an effective NLS equation makes use of the Bloch formalism, well known in solid-state physics. Even in the absence of nonlinear effects, the eigenfunctions associated with the photonic bands, corresponding to the dispersion relation  $q^2 = \delta^2 - \kappa^2$ , are not  $A_f$  and  $A_b$  but the Bloch waves formed by a linear combination of  $A_f$  and  $A_b$ . If this basis is used for the nonlinear problem, Eqs. (1.4.3) and (1.4.4) reduce to an effective NLS equation, provided two conditions are met. First, the peak intensity of the pulse is small enough that the nonlinear index change  $n_2 I_0$  in Eq. (1.3.1) is much smaller than the maximum value of  $\delta n_g$ . This condition is equivalent to requiring that  $\gamma P_0 \ll \kappa$  or  $\kappa L_{\text{NL}} \gg 1$ , where  $L_{\text{NL}} = (\gamma P_0)^{-1}$  is the nonlinear length. This requirement is easy to satisfy in practice, even at peak intensity levels as high as 100 GW/cm<sup>2</sup>. Second, the third-order dispersion  $\beta_3^g$  induced by the grating should be negligible.

When the preceding two conditions are satisfied, pulse propagation in a fiber grating is governed by the following NLS equation [117]:

$$\frac{i}{v_g} \frac{\partial U}{\partial t} - \frac{(1 - v^2)^{3/2}}{\text{sgn}(f) 2\kappa} \frac{\partial^2 U}{\partial \zeta^2} + \frac{1}{2} (3 - v^2) \gamma |U|^2 U, \quad (1.5.7)$$

where  $\zeta = z - V_G t$ . We have introduced a speed-reduction factor related to the parameter  $f$  through Eq. (1.4.6) as

$$v = \frac{V_G}{v_g} = \frac{1 - f^2}{1 + f^2} = \pm \sqrt{1 - \kappa^2 / \delta^2}. \quad (1.5.8)$$

The group velocity decreases by the factor  $v$  close to an edge of the stop band and vanishes at the two edges ( $v = 0$ ) corresponding to  $f = \pm 1$ . The reason the first term is a time derivative, rather than the  $z$  derivative, was discussed earlier. It can also be understood from a physical standpoint if we note that the variable  $U$  does not correspond to the amplitude of the forward- or backward-propagating wave but represents the amplitude of the envelope associated with the Bloch wave formed by a superposition of  $A_f$  and  $A_b$ .

Equation (1.5.7) has been written for the case in which the contribution of  $A_f$  dominates ( $|f| < 1$ ) so that the entire Bloch-wave envelope is propagating forward at the reduced group velocity  $V_G$ . With this in mind, we introduce  $z = V_G t$  as the distance traveled by the envelope and account for changes in its shape through a local time variable defined as  $T = t - z/V_G$ . Equation (1.5.8) can then be written in the following standard form of the NLS equation [2]:

$$i \frac{\partial U}{\partial z} - \frac{\beta_2^g}{2} \frac{\partial^2 U}{\partial T^2} + \gamma_g |U|^2 U = 0, \quad (1.5.9)$$

where the effective GVD parameter  $\beta_2^g$  and the nonlinear parameter  $\gamma_g$  are defined as

$$\beta_2^g = \frac{(1 - v^2)^{3/2}}{\text{sgn}(f) v_g^2 \kappa v^3}, \quad \gamma_g = \left( \frac{3 - v^2}{2v} \right) \gamma. \quad (1.5.10)$$

Using Eq. (1.5.8), the GVD parameter  $\beta_2^g$  can be shown to be the same as in Eq. (1.3.26).

Several features of Eq. (1.5.9) are noteworthy when this equation is compared with the standard NLS equation. First, the variable  $U$  represents the amplitude of the envelope associated with the Bloch wave formed by a superposition of  $A_f$  and  $A_b$ . Second, the parameters  $\beta_2^g$  and  $\gamma_g$  are not constants but depend on the speed-reduction factor  $v$ . Both increase as  $v$  decreases and become infinite at the edges of the stop band, where  $v = 0$ . Clearly, Eq. (1.5.9) is not valid at that point. However, it remains valid close to but outside of the stop band. Far from the stop band ( $v \rightarrow 1$ ),  $\beta_2^g$  becomes quite small ( $< 1$  ps<sup>2</sup>/km for typical values of  $\kappa$ ). One should then include fiber GVD and replace  $\beta_2^g$  by  $\beta_2$ . Noting that  $\gamma_g = \gamma$  when  $v = 1$ , Eq. (1.5.9) reduces to the standard NLS equation, and  $U$  corresponds to the forward-wave amplitude since no backward wave is generated under such conditions.

Before we can use Eq. (1.5.9) for predicting the modulation-instability gain and the frequency at which the gain peaks, we need to know the total power  $P_0$  inside the grating when a CW beam with power  $P_{\text{in}}$  is incident at the input end of the grating located at  $z = 0$ . This is a complicated issue for apodized fiber gratings, because  $\kappa$  is not constant in the transition or buffer zone. However, observing that the nonlinear coupled-mode equations require  $|A_f^2| - |A_b^2|$  to remain constant along the grating, one finds that the total power  $P_0$  inside the grating is enhanced by a factor  $1/v$  [124]. The predictions of Eq. (1.5.9) are in agreement with the modulation-instability analysis based on the nonlinear coupled-mode equations as long as  $\gamma P_0 \ll \kappa$  [117]. The NLS equation provides a shortcut to understanding the temporal dynamics in gratings within its regime of validity.

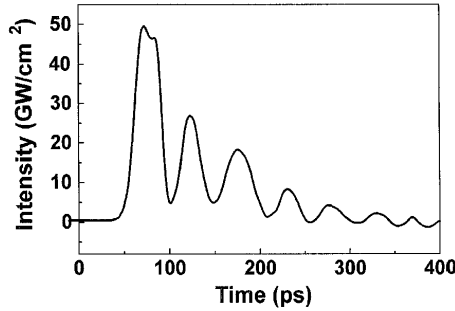


**Figure 1.16:** Transmitted pulse shape when 100-ps pulses with a peak intensity of  $25 \text{ GW/cm}^2$  are propagated through a 6-cm-long fiber grating. (From Ref. [124]; ©1998 Elsevier.)

### 1.5.3 Experimental Results

Modulation instability implies that an intense CW beam may get converted into a pulse train if it has passed through a fiber grating. The experimental observation of this phenomenon is difficult when a CW beam is used because the required input power is too large to be realistic. For this reason, experiments often use short optical pulses whose width is chosen to be much larger than the modulation period. In a 1996 experiment, 100-ps pulses—obtained from a Q-switched, mode-locked Nd:YLF laser operating close to  $1.053 \mu\text{m}$ —were used, and it was found that each pulse was transformed into two shorter pulses at the grating output [116]. The grating was only 3.5-cm long in this experiment and did not allow substantial growth of modulation instability.

In a 1998 experiment, a 6-cm-long fiber grating was used with a value of  $\kappa = 12 \text{ cm}^{-1}$  [124]. Figure 1.16 shows transmitted pulse shapes when 100-ps pulses were propagated through this grating. The peak intensity of the input Gaussian pulse is  $25 \text{ GW/cm}^2$ . Its central frequency is tuned close to but outside the stop band such that the grating provides anomalous GVD (upper branch of the dispersion curve). At lower power levels, the pulse is compressed because of the combination of GVD and SPM that leads to soliton-effect compression (discussed in Chapter 6). At the  $25 \text{ GW/cm}^2$  power level, the transmitted pulse exhibits a multipeak structure that can be interpreted as a pulse train generated through modulation instability. This interpretation is supported by the observation that the repetition rate (spacing between two neighboring pulses) changes with the laser wavelength (equivalent to changing the detuning parameter  $\delta$ ), as expected from the theory of modulation instability.

## 1.6 Nonlinear Pulse Propagation

It is well known that modulation instability often indicates the possibility of soliton formation [2]. In the case of Bragg gratings, it is closely related to a new kind of solitons referred to as *Bragg solitons* or *grating solitons*. Such solitons were first discovered in 1987 in the context of periodic structures known as superlattices [92] and were called *gap solitons*, since they existed only inside the stop band. Later, a

much larger class of Bragg solitons was identified by solving Eqs. (1.4.1) and (1.4.2) analytically [125]–[127].

The advent of fiber gratings during the 1990s provided an incentive for studying propagation of short optical pulses in such gratings [128]–[142]. The peak intensities required to observe the nonlinear effects are quite high (typically  $>10$  GW/cm<sup>2</sup>) for Bragg gratings made in silica fibers because of a short interaction length (typically  $<10$  cm) and a low value of the nonlinear parameter  $n_2$ . The use of chalcogenide glass fibers for making gratings can reduce required peak intensities by a factor of 100 or more because of the high values of  $n_2$  in such glasses [143].

### 1.6.1 Bragg Solitons

It was noted in 1989 that the coupled-mode equations, Eqs. (1.4.1) and (1.4.2), become identical to the well-known massive Thirring model [144] if the SPM term is set to zero. The massive Thirring model of quantum field theory is known to be integrable by the inverse scattering method [145]–[147]. When the SPM term is included, the coupled-mode equations become nonintegrable, and solitons do not exist in a strict mathematical sense. However, shape-preserving solitary waves can be obtained through a suitable transformation of the soliton supported by the massive Thirring model. These solitary waves correspond to the following solution [126]:

$$A_f(z, t) = a_+ \operatorname{sech}(\zeta - i\psi/2) e^{i\theta}, \quad (1.6.1)$$

$$A_b(z, t) = a_- \operatorname{sech}(\zeta + i\psi/2) e^{i\theta}, \quad (1.6.2)$$

where

$$a_{\pm} = \pm \left( \frac{1 \pm v}{1 \mp v} \right)^{1/4} \sqrt{\frac{\kappa(1-v^2)}{\gamma(3-v^2)}} \sin \psi, \quad \zeta = \frac{z - V_G t}{\sqrt{1-v^2}} \kappa \sin \psi, \quad (1.6.3)$$

$$\theta = \frac{v(z - V_G t)}{\sqrt{1-v^2}} \kappa \cos \psi - \frac{4v}{3-v^2} \tan^{-1} [|\cot(\psi/2)| \coth(\zeta)]. \quad (1.6.4)$$

This solution represents a two-parameter family of Bragg solitons. The parameter  $v$  lies in the range  $-1 < v < 1$  and the parameter  $\psi$  can be chosen anywhere in the range  $0 < \psi < \pi$ . The specific case  $\psi = \pi/2$  corresponds to the center of the stop band [125]. Physically, Bragg solitons represent specific combinations of counterpropagating waves that pair in such a way that they move at the same but reduced speed ( $V_G = vv_g$ ). Since  $v$  can be negative, the soliton can move forward or backward. The soliton width  $T_s$  is also related to the parameters  $v$  and  $\psi$  and is given by

$$T_s = \sqrt{1-v^2} / (\kappa V_G \sin \psi). \quad (1.6.5)$$

One can understand the reduced speed of a Bragg soliton by noting that the counterpropagating waves form a single entity that moves at a common speed. The relative amplitudes of the two waves participating in soliton formation determine the soliton speed. If  $A_f$  dominates, the soliton moves in the forward direction but at a reduced speed. The opposite happens when  $A_b$  is larger. In the case of equal amplitudes, the

soliton does not move at all since  $V_G$  becomes zero. This case corresponds to the stationary gap solitons predicted in the context of superlattices [92]. In the opposite limit, in which  $|v| \rightarrow 1$ , Bragg solitons cease to exist since the grating becomes ineffective.

Another family of solitary waves was obtained in 1993 by searching for the shape-preserving solutions of the nonlinear coupled-mode equations [127]. Such solitary waves exist both inside and outside the stop band. They reduce to the Bragg solitons described by Eqs. (1.6.2)–(1.6.4) in some specific limits. On the lower branch of the dispersion curve where the GVD is normal, solitary waves represent dark solitons, similar to those found for constant-index fibers [2].

## 1.6.2 Relation to NLS Solitons

As discussed earlier, the nonlinear coupled-mode equations reduce to the NLS equation when  $\gamma P_0 \ll \kappa$ , where  $P_0$  is the peak power of the pulse propagating inside the grating. Since the NLS equation is integrable by the inverse scattering method, the fundamental and higher-order solitons found with this method [2] should also exist for a fiber grating. The question then becomes how they are related to the Bragg soliton described by Eqs. (1.6.1) and (1.6.2).

To answer this question, we write the NLS equation (1.5.9) using soliton units in its standard form

$$i \frac{\partial u}{\partial \xi} + \frac{1}{2} \frac{\partial^2 u}{\partial \tau^2} + |u|^2 u = 0, \quad (1.6.6)$$

where  $\xi = z/L_D$ ,  $\tau = T/T_0$ ,  $u = \sqrt{\gamma_g L_D}$ , and  $L_D = T_0^2/|\beta_2^g|$  is the dispersion length. The fundamental soliton of this equation, in its most general form, is given by (see Section 5.2 of Ref. [2])

$$u(\xi, \tau) = \eta \operatorname{sech}[\eta(\tau - \tau_s + \varepsilon \xi)] \exp[i(\eta^2 - \varepsilon^2)\xi/2 - i\varepsilon\tau + i\phi_s], \quad (1.6.7)$$

where  $\eta$ ,  $\varepsilon$ ,  $\tau_s$ , and  $\phi_s$  are four arbitrary parameters representing amplitude, frequency, position, and phase of the soliton, respectively. The soliton width is related inversely to the amplitude as  $T_s = T_0/\eta$ . The physical origin of such solitons is the same as that for conventional solitons except that the GVD is provided by the grating rather than by material dispersion.

At first sight, Eq. (1.6.7) looks quite different than the Bragg soliton described by Eqs. (1.6.2)–(1.6.4). However, one should remember that  $u$  represents the amplitude of the Bloch wave formed by superimposing  $A_f$  and  $A_b$ . If the total optical field is considered and the low-power limit ( $\gamma P_0 \ll \kappa$ ) is taken, the Bragg soliton indeed reduces to the fundamental NLS soliton [101]. The massive Thirring model also allows for higher-order solitons [148]. One would expect them to be related to higher-order NLS solitons in the appropriate limit. It has been shown that any solution of the NLS equation (1.5.9) can be used to construct an approximate solution of the coupled-mode equations [123].

The observation that Bragg solitons are governed by an effective NLS equation in the limit  $\kappa L_{\text{NL}} \gg 1$ , where  $L_{\text{NL}}$  is the nonlinear length, allows us to use the concept of soliton order  $N$  and the soliton period  $z_0$  developed in Chapter 5 of Ref. [2]. These

parameters are defined as

$$N^2 = \frac{L_D}{L_{\text{NL}}} \equiv \frac{\gamma_g P_0 T_0^2}{|\beta_2^g|}, \quad z_0 = \frac{\pi}{2} L_D \equiv \frac{\pi}{2} \frac{T_0^2}{|\beta_2^g|}. \quad (1.6.8)$$

We need to interpret the meaning of the soliton peak power  $P_0$  carefully since the NLS soliton represents the amplitude of the Bloch wave formed by a combination of  $A_f$  and  $A_b$ . This aspect is discussed later in this section.

An interesting issue is related to the collision of Bragg solitons. Since Bragg solitons described by Eqs. (1.6.1) and (1.6.2) are only solitary waves (because of the nonintegrability of the underlying nonlinear coupled-mode equations), they may not survive collisions. On the other hand, the NLS solitons are guaranteed to remain unaffected by their mutual collisions. Numerical simulations based on Eqs. (1.4.1) and (1.4.2) show that Bragg solitons indeed exhibit features reminiscent of a NLS soliton in the low-power limit  $\gamma P_0 \ll \kappa$  [136]. More specifically, two Bragg solitons attract or repel each other depending on their relative phase. The new feature is that the relative phase depends on the initial separation between the two solitons.

### 1.6.3 Formation of Bragg Solitons

Formation of Bragg solitons in fiber gratings was first observed in a 1996 experiment [128]. Since then, more careful experiments have been performed, and many features of Bragg solitons have been extracted. While comparing the experimental results with the coupled-mode theory, one needs to implement the boundary conditions properly. For example, the peak power  $P_0$  of the Bragg soliton formed inside the grating when a pulse is launched is not the same as the input peak power  $P_{\text{in}}$ . The reason can be understood by noting that the group velocity of the pulse changes as the input pulse crosses the front end of the grating located at  $z = 0$ . As a result, pulse length given by  $v_g T_0$  just outside the grating changes to  $V_G T_0$  on crossing the interface located at  $z = 0$  [80], and the pulse peak power is enhanced by the ratio  $v_g/V_G$ . Mathematically, one can use the coupled-mode equations to show that  $P_0 = |A_f^2| + |A_b^2| = P_{\text{in}}/v$ , where  $v = V_G/v_g$  is the speed-reduction factor introduced earlier. The argument becomes more complicated for apodized fiber gratings, used often in practice, because  $\kappa$  is not constant in the transition region [133]. However, the same power enhancement occurs at the end of the transition region.

From a practical standpoint, one needs to know the amount of peak power  $P_{\text{in}}$  required to excite the fundamental Bragg soliton. The soliton period  $z_0$  is another important parameter relevant for soliton formation since it sets the length scale over which optical solitons evolve. We can use Eq. (1.6.8) with  $N = 1$  to estimate both of them. Using the expressions for  $\beta_2^g$  and  $\gamma_g$  from Eq. (1.5.10), the input peak power and the soliton period are given by

$$P_{\text{in}} = \frac{2(1-v^2)^{3/2}}{v(3-v^2)v_g^2 T_0^2 \kappa \gamma}, \quad z_0 = \frac{\pi v^3 v_g^2 T_0^2 \kappa}{2(1-v^2)^{3/2}}, \quad (1.6.9)$$

where  $T_0$  is related to the FWHM as  $T_{\text{FWHM}} \approx 1.76T_0$ . Both  $P_{\text{in}}$  and  $z_0$  depend through  $v$  on detuning of the laser wavelength from the edge of the stop band located at  $\delta = \kappa$ . As  $v \rightarrow 0$  near the edge,  $P_{\text{in}}$  becomes infinitely large while  $z_0$  tends toward zero.

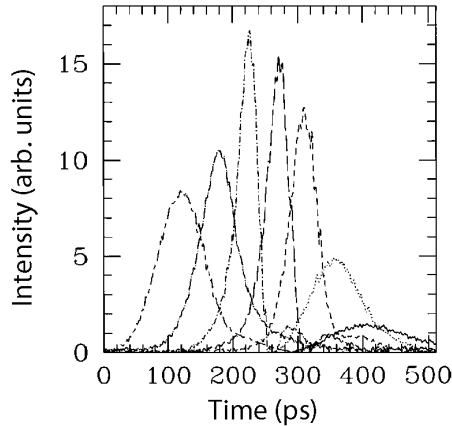


**Figure 1.17:** Output pulse shapes for different  $\delta$  when 80-ps pulses with a peak intensity of  $11 \text{ GW/cm}^2$  are propagated through a 7.5-cm-long fiber grating. Values of  $\delta$  from left to right are 3612, 1406, 1053, 935, 847, 788, and  $729 \text{ m}^{-1}$ . (From Ref. [88]; ©1999 OSA.)

In a 1999 experiment, Bragg solitons were formed inside a 7.5-cm-long apodized fiber grating by launching 80-ps pulses, obtained from a Q-switched, mode-locked Nd:YLF laser operating at 1053 nm [88]. Figure 1.17 shows pulse shapes observed at the output end of the grating when input pulses with a peak intensity of  $11 \text{ GW/cm}^2$  were used. The coupling coefficient  $\kappa$  was estimated to be  $7 \text{ cm}^{-1}$  for this grating. The detuning parameter  $\delta$  was varied in the range of 7 to  $36 \text{ cm}^{-1}$  on the blue side of the stop band (anomalous GVD). The arrival time of the pulse depends on  $\delta$  because of a decrease in its group velocity occurring as  $\delta$  is tuned closer to the stop-band edge. This delay occurs even when nonlinear effects are negligible as shown in Figure 1.11, which was obtained under identical operating conditions, but at a much lower value of the peak intensity.

At the high peak intensities used for Figure 1.17, SPM in combination with the grating-induced anomalous GVD leads to formation of Bragg solitons. However, since both  $\beta_2^g$  and  $\gamma_g$  depend on the detuning parameter  $\delta$  through  $v$ , a Bragg soliton can form only in a limited range of  $\delta$ . With this in mind, we can understand the pulse shapes seen in Figure 1.17. Detuning is so large and  $\beta_2^g$  is so small for the leftmost trace that the pulse acquires some chirping through SPM but its shape remains nearly unchanged. This feature can also be understood from Eq. (1.6.9), where the soliton period becomes so long as  $v \rightarrow 1$  that nothing much happens to the pulse over a few-cm-long grating. As  $\delta$  is reduced, the pulse narrows down considerably. A reduction in pulse width by a factor of 3 occurs for  $\delta = 1053 \text{ m}^{-1}$  in Figure 1.17. This pulse narrowing is an indication that a Bragg soliton is beginning to form. However, the soliton period is still much longer than the grating length. In other words, the grating is not long enough to observe the final steady-state shape of the Bragg soliton. Finally, as the edge of the stop band is approached and  $\delta$  becomes comparable to  $\kappa$  (rightmost solid trace), the GVD becomes so large that the pulse cannot form a soliton and becomes broader than the input pulse. This behavior is also deduced from Eq. (1.6.8), which shows that both

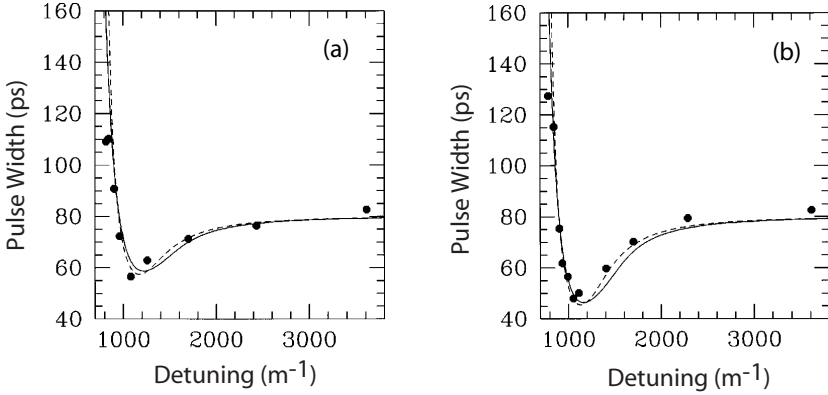


**Figure 1.18:** Measured pulse widths (circles) as a function of detuning for 80-ps input pulses with a peak intensity of (a) 3 GW/cm<sup>2</sup> and (b) 6 GW/cm<sup>2</sup>. Predictions of the coupled-mode theory (solid line) and the effective NLS equation (dashed line) are shown for comparison. (From Ref. [88]; ©1999 OSA.)

$N$  and  $z_0$  tend toward zero as  $\beta_2^s$  tends toward infinity. A Bragg soliton can form only if  $N > \frac{1}{2}$ . Since the dispersion length becomes smaller than the grating length close to the stop-band edge, pulse can experience considerable broadening. This is precisely what is observed for the smallest value of  $\delta$  in Figure 1.17 (solid curve).

A similar behavior was observed over a large range of pulse energies, with some evidence of the second-order soliton for input peak intensities in excess of 20 GW/cm<sup>2</sup> [88]. A careful comparison of the experimental data with the theory based on the nonlinear coupled-mode equations and the effective NLS equation showed that the NLS equation provides an accurate description within its regime of validity. Figure 1.18 compares the measured values of the pulse width with the two theoretical models for peak intensities of 3 and 6 GW/cm<sup>2</sup>. The NLS equation is valid as long as  $\kappa L_{NL} \gg 1$ . Using  $\kappa = 7 \text{ cm}^{-1}$ , we estimate that the peak intensity can be as high as 50 GW/cm<sup>2</sup> for the NLS equation to remain valid. This is also what was found in Ref. [88].

Gap solitons that form within the stop band of a fiber grating have not been observed because of a practical difficulty: A Bragg grating reflects light whose wavelength falls inside the stop band. Stimulated Raman scattering may provide a solution to this problem, since a pump pulse, launched at a wavelength far from the stop band, can excite a “Raman gap soliton” that is trapped within the grating and propagates much more slowly than the pump pulse itself [138]. The energy of such a gap soliton leaks slowly from the grating ends, but it can survive for durations greater than 10 ns even though it is excited by pump pulses of duration 100 ps or so.

### 1.6.4 Nonlinear Switching

As discussed in Section 1.4.2, a fiber grating can exhibit bistable switching even when a CW beam is incident on it. However, optical pulses should be used in practice because of the high intensities required for observing SPM-induced nonlinear switching.

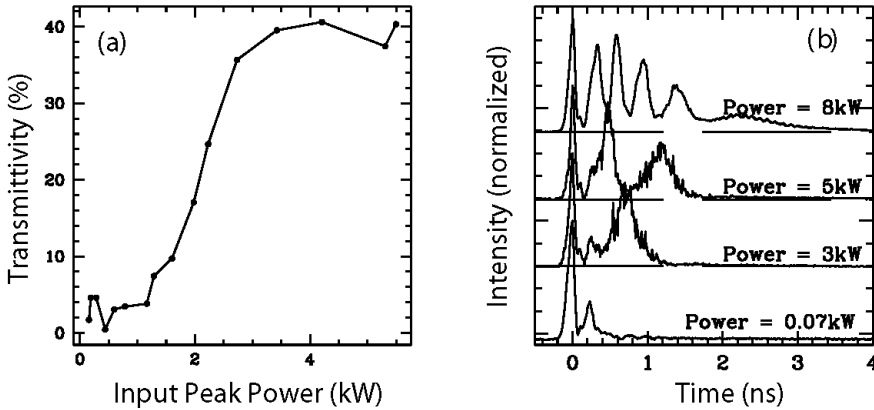


**Figure 1.19:** (a) Transmittivity as a function of input peak power showing nonlinear switching; (b) output pulse shapes at several peak power levels. (From Ref. [134]; ©1998 OSA.)

Even then, one needs peak-intensity values in excess of  $10 \text{ GW/cm}^2$ . For this reason, bistable switching was first observed during the 1980s using DFB semiconductor amplifiers for which large carrier-induced nonlinearities reduce the switching threshold to power levels below  $1 \text{ mW}$  [149]–[151]. Nonlinear switching in a passive grating was observed in a 1992 experiment using a semiconductor waveguide grating [98]. The nonlinear response of such gratings is not governed by the Kerr-type nonlinearity seen in Eq. (1.3.1) because of the presence of free carriers (electrons and holes) whose finite lifetime limits the nonlinear response time.

Nonlinear switching in a fiber Bragg grating was observed in 1998 in the  $1.55\text{-}\mu\text{m}$  wavelength region useful for fiber-optic communications [132]. An 8-cm-long grating, with its Bragg wavelength centered near  $1536 \text{ nm}$ , was used in the experiment. It had a peak reflectivity of 98% and its stop band was only 4 GHz wide. The 3-ns input pulses were obtained by amplifying the output of a pulsed DFB semiconductor laser to power levels as high as  $100 \text{ kW}$ . Their shape was highly asymmetric because of gain saturation occurring inside the amplifier chain. The laser wavelength was inside the stop band on the short-wavelength side but was set very close to the edge (offset of about  $7 \text{ pm}$  or  $0.9 \text{ GHz}$ ).

Figure 1.19(a) shows a sharp rise in the transmittivity from a few percent to 40% when the peak power of input pulses increases beyond  $2 \text{ kW}$ . Physically, the nonlinear increase in the refractive index at high powers shifts the Bragg wavelength far enough that the pulse finds itself outside the stop band and switches to the upper branch of the bistability curves seen in Figure 1.13. The pulse shapes seen in Figure 1.19(b) show what happens to the transmitted pulse. The initial spike near  $t = 0$  in these traces is due to a sharp leading edge of the asymmetric input pulse and should be ignored. Multiple pulses form at the grating output, whose number depends on the input power level. At a power level of  $3 \text{ kW}$ , a single pulse is seen but the number increases to five at a power level of  $8 \text{ kW}$ . The pulse width is smallest (about  $100 \text{ ps}$ ) near the leading edge of the pulse train but increases substantially for pulses near the trailing edge.

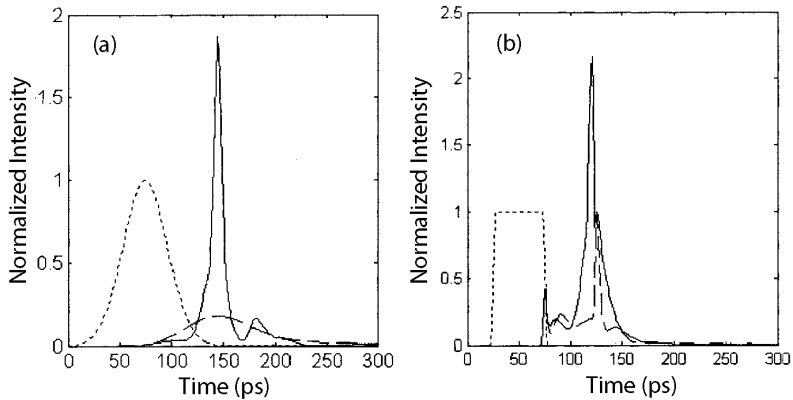


**Figure 1.20:** Transmitted pulse shapes in the on (solid curves) and off (dashed curves) states when 50-ps (a) Gaussian and (b) square input pulses (dotted curves) are transmitted through a fiber grating with  $\kappa L = 4$ . (From Ref. [139]; ©2003 IEEE.)

Several conclusions can be drawn from these results. First, the upper bistability branch in Figure 1.13 is not stable and converts the quasi-CW signal into a pulse train [90]. Second, each pulse evolves toward a constant width. Pulses near the leading edge have had enough propagation time within the grating to stabilize their widths. These pulses can be thought of as a gap soliton since they are formed even though the input signal is inside the photonic bandgap and would be completely reflected in the absence of the nonlinear effects. Third, pulses near the trailing edge are wider simply because the fiber grating is not long enough for them to evolve completely toward a gap soliton. This interpretation was supported by a later experiment in which the grating length was increased to 20 cm [137]. Six gap solitons were found to form in this grating at a peak power level of 1.8 W. The observed data were in agreement with theory based on the nonlinear coupled-mode equations.

In a 2003 study, numerical simulations were used to characterize the nonlinear switching characteristics of a wide variety of pulses of different widths and shape through uniform as well as phase-shifted fiber gratings [139]. The bistable behavior, similar to that seen in Figure 1.13 for CW beams, is realized only for pulses wider than 10 ns. The use of phase-shifted gratings reduces the switching threshold, but the on-off contrast is generally better for uniform gratings. For short pulses (width  $< 1$  ns), launched such that most of their spectrum lies inside the stop band of the grating initially, almost the entire input energy is transmitted in the form of a compressed optical pulse, once the peak-power level is large enough to switch the pulse to the “on” branch. Moreover, the shape of output pulse depends strongly on the rise and fall times associated with the pulses tails. Figure 1.20 shows the transmitted pulse shapes in the on (solid curves) and off (dashed curves) states when 50-ps Gaussian or square input pulses (dotted curves) are transmitted through a fiber grating with  $\kappa L = 4$ . Although nonlinear switching occurs in both cases, the pulse quality is better in the case of Gaussian pulses. In particular, a grating can be used to compress short optical pulses. In a 2005 experiment, 580-ps pulses with 1.4-kW peak power could be compressed down

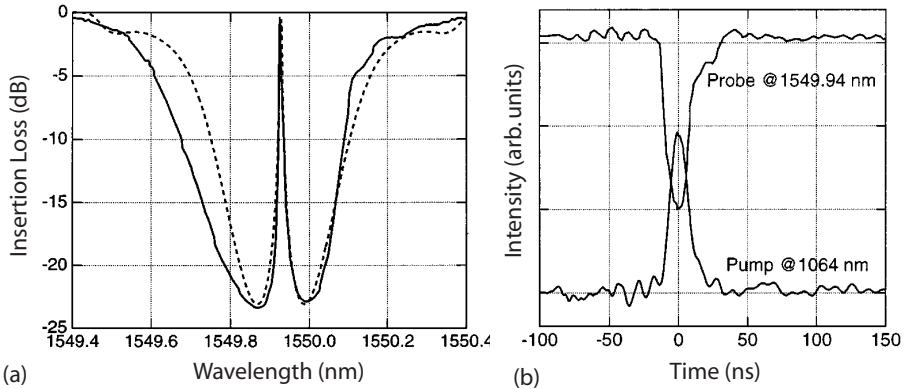


**Figure 1.21:** (a) Measured (solid) and calculated (dashed) transmittivity of the 2-cm-long phase-shifted fiber grating. (b) Pump and probe intensity profiles showing XPM-induced nonlinear switching. (From Ref. [154]; ©2000 IEEE.)

to 45 ps by launching them into a 10-cm-long apodized fiber grating [141].

The nonlinear switching seen in Figure 1.19 is sometimes called *SPM-induced* or *self-induced switching*, since the pulse changes the refractive index to switch itself to the high-transmission state. Clearly, another signal at a different wavelength can also induce switching of the pulse by changing the refractive index through XPM, resulting in XPM-induced switching. This phenomenon was first observed in 1990 as an increase in the transmittivity of a 514-nm signal caused by a 1064-nm pump beam [96]. The increase in transmission was less than 10% in this experiment.

It was suggested later that XPM could be used to form a “push broom” such that a weak CW beam (or a broad pulse) would be swept by a strong pump pulse and its energy piled up at the front end of the pump pulse [152]. The basic idea behind the optical push broom is quite simple. If the wavelength of the pump pulse is far from the stop band while that of the probe is close to but outside the stop band (on the lower branch of the dispersion curve), the pump travels faster than the probe. In the region where the pump and probe overlap, the XPM-induced chirp changes the probe frequency such that it moves with the leading edge of the pump pulse. As the pump pulse travels further, it sweeps more and more of the probe energy and piles it up at its leading edge. In effect, the pump acts like a push broom. At the grating output, a significant portion of the probe energy appears at the same time as the pump pulse in the form of a sharp spike because of the XPM-induced increase in the probe speed. Such a push-broom effect has been seen in a 1997 experiment [153].

In a 2000 experiment, a phase-shifted fiber grating was used to realize XPM-induced nonlinear switching at relatively low power levels [154]. In this pump–probe experiment, a 1550-nm CW laser was tuned precisely to the center of the stop band associated with the 2-cm-long grating so that it was fully transmitted by the narrow transmission peak seen in Figure 1.21(a). When a pump pulse (width  $\sim 10$  ns) from a Nd:YAG laser operating at 1064 nm was launched with the probe, the probe power dropped considerably over the temporal window of the pulse, as seen in Figure 1.21(b).

This switching is due to the XPM-induced shift of the probe spectrum. Even a relatively small shift moves the probe outside the narrow transmission peak, resulting in a drop in its transmissivity through the grating. The switching could be observed at a relatively low power level of 730 W because of the use of a phase-shifted fiber grating.

### 1.6.5 Effects of Birefringence

As discussed in Chapter 6 of Ref. [2], fiber birefringence plays an important role and affects the nonlinear phenomena considerably. Its effects should be included if Bragg gratings are made inside the core of polarization-maintaining fibers. The coupled-mode theory can be easily extended to account for fiber birefringence [155]–[158]. However, the problem becomes quite complicated, since one needs to solve a set of four coupled equations describing the evolution of two orthogonally polarized components, each containing both the forward- and backward-propagating waves. This complexity, however, leads to a rich class of nonlinear phenomena with practical applications such as optical logic gates.

From a physical viewpoint, the two orthogonally polarized components have slightly different mode indices. Since the Bragg wavelength depends on the mode index, the stop bands of the two modes have the same widths but are shifted by a small amount with respect to each other. As a result, even though both polarization components have the same wavelength (or frequency), one of them may fall inside the stop band while the other remains outside it. Moreover, as the two stop bands shift due to nonlinear index changes, the shift can be different for the two orthogonally polarized components because of the combination of the XPM and birefringence effects. It is this feature that leads to a variety of interesting nonlinear effects.

In the case of CW beams, the set of four coupled equations was solved numerically in 1994 and several birefringence-related nonlinear effects were identified [156]. One such effect is related to the onset of polarization instability discussed in Section 6.3 of Ref. [2]. The critical power at which this instability occurs is reduced considerably in the presence of a Bragg grating [159]. Nonlinear birefringence also affects Bragg solitons. In the NLS limit ( $\gamma P_0 \ll \kappa$ ), the four equations reduce a pair of coupled NLS equations. In the case of low-birefringence fibers, the two polarization components have nearly the same group velocity, and the coupled NLS equations take the following form [155]:

$$\frac{\partial A_x}{\partial z} + \frac{i\beta_2^g}{2} \frac{\partial^2 A_x}{\partial T^2} = i\gamma_g \left( |A_x|^2 + \frac{2}{3}|A_y|^2 \right) A_x + \frac{i\gamma_g}{3} A_x^* A_y^2 e^{-2i\Delta\beta z}, \quad (1.6.10)$$

$$\frac{\partial A_y}{\partial z} + \frac{i\beta_2^g}{2} \frac{\partial^2 A_y}{\partial T^2} = i\gamma_g \left( |A_y|^2 + \frac{2}{3}|A_x|^2 \right) A_y + \frac{i\gamma_g}{3} A_y^* A_x^2 e^{2i\Delta\beta z}, \quad (1.6.11)$$

where  $\Delta\beta \equiv \beta_{0x} - \beta_{0y}$  is related to the beat length  $L_B$  as  $\Delta\beta = 2\pi/L_B$ . These equations support a vector soliton with equal amplitudes, such that the peak power required for each component is only  $\sqrt{3/5}$  of that required when only one component is present. Such a vector soliton is referred to as the *coupled-gap soliton* [155].

The coupled-gap soliton can be used for making an all-optical AND gate. The  $x$  and  $y$  polarized components of the input light represent bits for the gate, each bit taking a

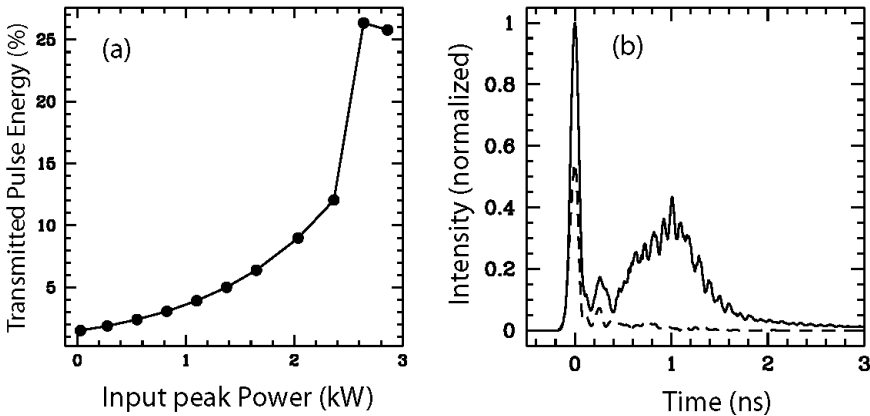


**Figure 1.22:** (a) Grating transmissivity as a function of input peak power showing the operation of the AND gate and (b) output pulse shapes at a peak power level of 3 kW, when only one polarization component (dashed line) or both polarization components (solid line) are incident at the input end. (From Ref. [134]; ©1998 OSA.)

value of 0 or 1 depending on whether the corresponding signal is absent or present. The AND gate requires that a pulse appears at the output only when both components are present simultaneously. This can be achieved by tuning both polarization components inside the stop band but close to the upper branch of the dispersion curve. Their combined intensity can increase the refractive index (through a combination of SPM and XPM) enough that both components are transmitted. However, if one of the components is absent at the input (0 bit), the XPM contribution vanishes and both components are reflected by the grating. This occurs simply because the coupled gap soliton forms at a lower peak power level than the Bragg soliton associated with each individual component [155].

An all-optical AND gate was realized in a 1998 experiment in which a switching contrast of 17 dB was obtained at a peak power level of 2.5 kW [131]. Figure 1.22 shows the fraction of total pulse energy transmitted (a) as a function of input peak power and the transmitted pulse shapes (b) at a peak power of 3 kW. When only one polarization component is incident at the input end, little energy is transmitted by the grating. However, when both polarization components are launched, each having the same peak power, an intense pulse is seen at the output end of the grating, in agreement with the prediction of the coupled NLS equations.

The XPM-induced coupling can be advantageous even when the two polarization components have different wavelengths. For example, it can be used to switch the transmission of a CW probe from low to high by using an orthogonally polarized short pump pulse at a wavelength far from the stop band associated with the probe [160]. In contrast with the self-induced bistable switching discussed earlier, XPM-induced bistable switching can occur for a CW probe too weak to switch itself. Furthermore, the short pump pulse switches the probe beam permanently to the high-transmission state.

## 1.7 Related Periodic Structures

This chapter has so far focused on uniform Bragg gratings (except for apodization) that are designed to couple the forward- and backward-propagating waves inside an optical fiber. Many variations of this simple structure exist. In this section, we consider several other kinds of gratings and discuss the nonlinear effects occurring when intense light propagates through them.

### 1.7.1 Long-Period Gratings

Long-period gratings are designed to couple the fundamental fiber mode to a higher-order copropagating mode [161]–[167]. In the case of a single-mode fiber, the higher-order mode propagates inside the cladding and is called a *cladding mode*. The grating period required for coupling the two copropagating modes can be calculated from Eq. (1.1.2) and is given by  $\Lambda = \lambda / \Delta n$ , where  $\Delta n$  is the difference in the refractive indices of the two modes coupled by the grating. Since  $\Delta n \sim 0.01$  typically,  $\Lambda$  is much larger than the optical wavelength. For this reason, such gratings are called *long-period gratings*.

The coupled-mode theory of Section 1.3 can be used for long-period gratings. In fact, the resulting equations are similar to Eqs. (1.3.11) and (1.3.12) and can be written as [163]

$$\frac{\partial A_1}{\partial z} + \frac{1}{v_{g1}} \frac{\partial A_1}{\partial t} + \frac{i\beta_{21}}{2} \frac{\partial^2 A_1}{\partial t^2} = i\delta A_1 + i\kappa A_2 + i\gamma_1(|A_1|^2 + c_1|A_2|^2)A_1, \quad (1.7.1)$$

$$\frac{\partial A_2}{\partial z} + \frac{1}{v_{g2}} \frac{\partial A_2}{\partial t} + \frac{i\beta_{22}}{2} \frac{\partial^2 A_2}{\partial t^2} = i\delta A_2 + i\kappa A_1 + i\gamma_2(|A_2|^2 + c_2|A_1|^2)A_2, \quad (1.7.2)$$

where  $A_1$  and  $A_2$  represent the slowly varying amplitudes of the two copropagating modes coupled by the grating. A comparison of these equations with Eqs. (1.3.11) and (1.3.12) reveals several important differences. First, the two  $z$  derivatives have the same sign, since both waves travel in the forward direction. Second, the group velocities and the GVD parameters can be different for the two modes, because of their different mode indices. Third, the SPM parameters  $\gamma_j$  and the XPM parameters  $c_j$  are also generally different for  $j = 1$  and  $2$ . The reason is related to different spatial profiles for the two modes, resulting in different overlap factors.

In the case of low-power CW beams, both the nonlinear and the GVD effects can be neglected in Eqs. (1.7.1) and (1.7.2) by setting  $\gamma_j = 0$  and  $\beta_2 = 0$  ( $j = 1, 2$ ). These equations then reduce to Eqs. (1.3.13) and (1.3.14), with the only difference being that both  $z$  derivatives have the same sign. They can be solved readily and exhibit features similar to those discussed in Section 1.3.2. When a single beam excites the  $A_1$  mode at the fiber input, its transmission depends on its detuning  $\delta$  from the Bragg wavelength and becomes quite small within the stop band centered at  $\delta = 0$ . The reason is easily understood by noting that the grating transfers power to the  $A_2$  mode as light propagates inside the grating.

The nonlinear effects such as SPM and XPM can affect the amount of power transferred by changing the refractive index and shifting the Bragg wavelength toward longer wavelengths. As a result, a long-period grating should exhibit nonlinear

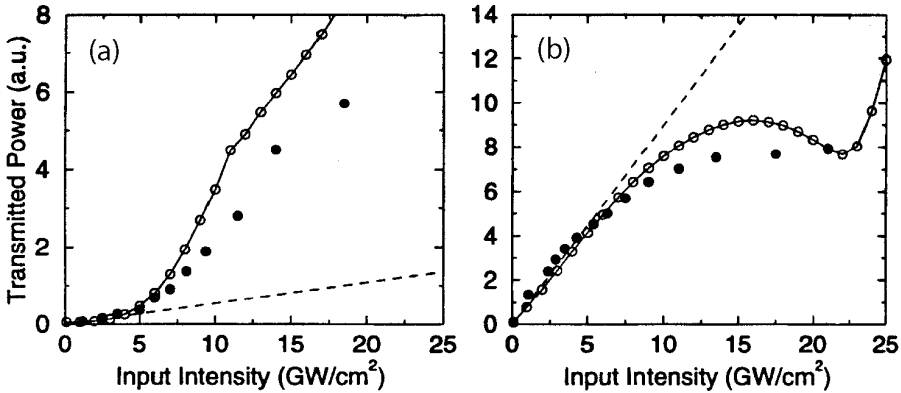


**Figure 1.23:** Transmitted power as a function of input peak power for (a)  $\delta = 0$  and (b)  $-1.5 \text{ cm}^{-1}$ . Experimental data (solid circles) are compared with coupled-mode theory (open circles). Dashed lines show the behavior expected in the absence of nonlinear effects. (From Ref. [163]; ©1997 IEEE.)

switching. Moreover, the switching intensity is expected to be lower by a factor of  $\bar{n}/\Delta n \sim 100$  compared with that required for short-period Bragg gratings. Figure 1.23 shows nonlinear changes in the transmitted power as a function of input peak intensity when 70-ps Gaussian pulses are transmitted through a 5-cm-long grating and compares the experimental data with the prediction of coupled-mode theory. Dashed lines show the linear increase in transmission expected in the absence of nonlinear effects. For  $\delta = 0$  [Figure 1.23(a)], the input wavelength coincides with the Bragg wavelength, and little transmission occurs in the linear case. However, at intensity levels beyond  $5 \text{ GW/cm}^2$ , the nonlinear effects shift the Bragg wavelength enough that a significant part of the incident power is transmitted through the grating. When the input wavelength is detuned by about 5.2 nm from the Bragg wavelength ( $\delta = -1.5 \text{ cm}^{-1}$ ), the transmitted power decreases at high peak intensities, as seen in Figure 1.23(b).

Considerable pulse shaping was observed in the preceding experiment because of the use of short optical pulses. This feature can be used to advantage to compress and reshape an optical pulse. Nonlinear effects in long-period fiber gratings are likely to remain important and find practical applications.

## 1.7.2 Nonuniform Bragg Gratings

Both the linear and nonlinear properties of a Bragg grating can be considerably modified by introducing nonuniformities along its length [105]. Examples of such nonuniform gratings include chirped gratings, phase-shifted gratings, and superstructure gratings. The refractive index in such gratings still has the general form of Eq. (1.3.1), but its periodic part  $\delta n_g(z)$  is modified to become

$$\delta n_g(z) = \delta n_1(z) \cos[2\pi z/\Lambda(z) + \phi(z)], \quad (1.7.3)$$

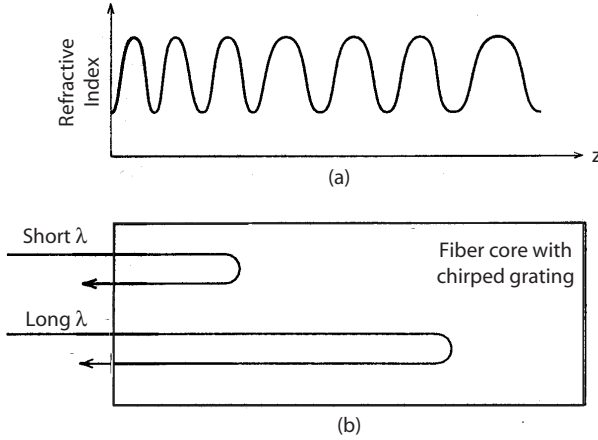


**Figure 1.24:** (a) Variations of refractive index in a chirped fiber grating. (b) Short and long wavelength components of a pulse are reflected at different locations within the grating because of variations in the Bragg wavelength.

where  $\delta n_1$ ,  $\phi$ ,  $\Lambda$ , or a combination of them depends on  $z$ . If  $\delta n_1$  varies with  $z$ , the coupling coefficient  $\kappa$  becomes  $z$  dependent (as in an apodized grating). In a chirped grating, the grating period  $\Lambda$  varies along the grating length as shown in Figure 1.24. In a phase-shifted grating, the phase  $\phi$  is changed abruptly by  $\pi/2$  in the middle of an otherwise uniform grating. It was seen in Section 1.4.2 that the use of a phase-shifted grating can reduce the switching power by a factor of 100 or more. In this section, we focus on chirped and other nonuniform gratings.

In a chirped grating, the index-modulation period  $\bar{n}\Lambda$  changes along the fiber length. Since the Bragg wavelength ( $\lambda_B = 2\bar{n}\Lambda$ ) sets the frequency at which the stop band is centered, axial variations of  $\bar{n}$  or  $\Lambda$  translate into a shift of the stop band along the grating length. Mathematically, the parameter  $\delta$  appearing in the nonlinear coupled-mode equations becomes  $z$  dependent. Typically,  $\Lambda$  is designed to vary linearly along the grating, resulting in  $\delta(z) = \delta_0 + \delta_c z$ , where  $\delta_c$  is a chirp parameter. Such gratings are called linearly chirped gratings.

Chirped fiber gratings can be fabricated using several methods [48]. It is important to note that it is the optical period  $\bar{n}\Lambda$  that needs to be varied along the grating length ( $z$  axis). Thus, chirping can be induced either by varying the physical grating period  $\Lambda$  or by changing the effective mode index  $\bar{n}$  along  $z$ . In the commonly used dual-beam holographic technique, the fringe spacing of the interference pattern is made nonuniform by using dissimilar curvatures for the interfering wavefronts, resulting in  $\Lambda$  variations. In practice, cylindrical lenses are used in one or both arms of the interferometer. Chirped fiber gratings can also be fabricated by tilting or stretching the fiber, by using strain or temperature gradients, or by stitching together multiple uniform sections.

Chirped Bragg gratings have several important practical applications. As shown in Figure 1.24, when a pulse, with its spectrum inside the stop band, is incident on a

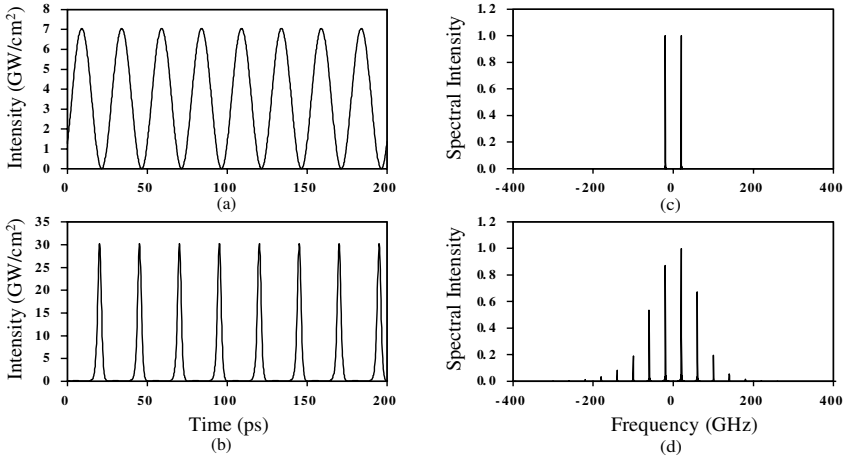


**Figure 1.25:** Temporal signal [(a) and (b)] and its spectrum [(c) and (d)] at the input [(a) and (c)] and output [(b) and (d)] end of a fiber grating designed with a linearly decreasing  $\kappa$ . (From Ref. [172]; ©1998 OSA.)

chirped grating, different spectral components of the pulse are reflected by different parts of the grating. As a result, even though the entire pulse is eventually reflected, it experiences a large amount of GVD, whose nature (normal versus anomalous) and magnitude can be controlled by the chirp. For this reason, chirped gratings are commonly used for dispersion compensation [87] and pulse compression [168]–[170]. The latter topic is discussed in Chapter 6. Chirped gratings also exhibit interesting non-linear effects when the incident pulse is sufficiently intense. In one experiment, 80-ps pulses were propagated through a 6-cm-long grating whose linear chirp could be varied over a considerable range through a temperature gradient established along its length [171]. The reflected pulses were split into a pair of pulses by the combination of SPM and XPM for peak intensities close to  $10 \text{ GW/cm}^2$ .

When  $\delta n_1$  in Eq. (1.7.3) varies with  $z$ , the coupling coefficient  $\kappa$  becomes nonuniform along the grating length. In practice, variations in the intensity of the ultraviolet laser beam used to make the grating translate into axial variations of  $\kappa$ . From a physical standpoint, since the width of the photonic bandgap is about  $2\kappa$ , changes in  $\kappa$  result into changes in the width of the stop band along the grating length. At a fixed wavelength of input light, such local variations in  $\kappa$  lead to axial variations of the group velocity  $V_G$  and the GVD parameter  $\beta_2^g$ , as seen from Eqs. (1.3.25) and (1.3.26), respectively. In effect, the dispersion provided by the grating becomes nonuniform and varies along its length. Such gratings can have a number of applications. For example, they can be used to generate pulse trains at high repetition rates by launching the output of two CW lasers with closely spaced wavelengths.

Figure 1.25 shows the numerical results obtained by solving Eqs. (1.4.1) and (1.4.2) with  $\kappa(z) = \kappa_0(1 - \kappa_1 z)$  for the case in which laser frequencies are 40 GHz apart [172]. The grating is assumed to be 70 cm long with parameters  $\kappa_0 = 70 \text{ cm}^{-1}$  and  $\delta = 160 \text{ cm}^{-1}$ . The parameter  $\kappa_1$  is chosen such that the index changes seen at the begin-

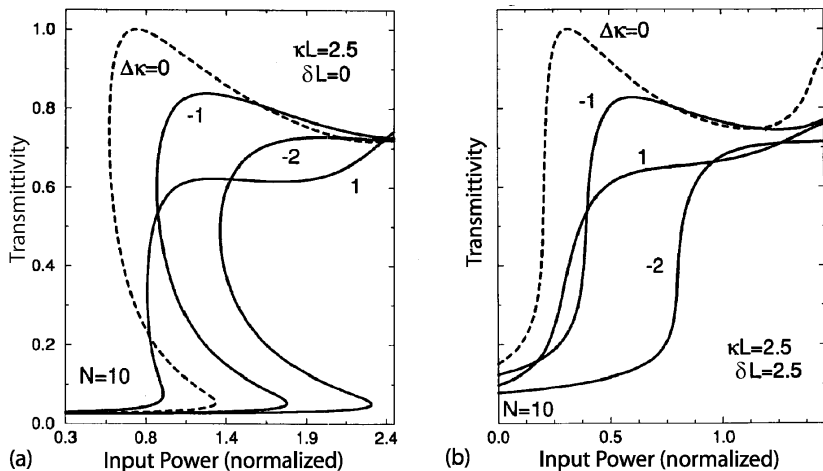


**Figure 1.26:** transmittivity of a CW signal as a function of its input intensity (normalized) for two values  $\delta L=0$  or  $2.5$  when  $\kappa L$  varies linearly over the grating length. (From Ref. [105]; ©1995 IEEE.)

ning of the grating are reduced by a factor of 5 at the end of the grating. The pulse compression can be understood by noting that the nonlinear effects (SPM and XPM) chirp the pulse and broaden its spectrum, and the GVD compresses the chirped pulse. It can also be thought of in terms of a four-wave mixing process, phase-matched by the nonlinearity, which generates multiple sidebands at the grating output, as seen in Figure 1.25.

The nonlinear switching characteristics of nonuniform gratings were first studied in 1995 using a transfer-matrix method [105]. A different technique was employed in a 2004 study, yielding the same results [173]. As an example, Figure 1.26 shows the transmittivity of a CW signal as a function of its input power [normalized to  $P_c = (\gamma L)^{-1}$ ] for two values of detuning such that  $\delta L = 0$  or  $2.5$ . The coupling coefficient of the grating is tapered linearly such that  $\kappa(z) = \kappa[1 + \Delta\kappa(z/L - \frac{1}{2})]$ . In general, tapering of  $\kappa$  modifies the bistable characteristics and affects the power level at which the CW beam switches back and forth between the on and off states.

In another class of gratings, the grating parameters  $\kappa$  and  $\delta$  are designed to vary periodically along the length of a grating. Such devices have double periodicity and are called *sampled* or *superstructure gratings*. They were first used in the context of DFB semiconductor lasers [174]. Fiber-based sampled gratings were made in 1994 [175]. Since then, their properties have attracted considerable attention [176]–[184]. A simple example of a superstructure grating is provided by a long grating in which constant phase-shift regions occur at periodic intervals. In practice, such a structure can be realized by placing multiple gratings next to each other with a small constant spacing between them or by blocking small regions during fabrication of a grating such that  $\kappa = 0$  in the blocked regions. In a phase-sampled grating [182]–[184], the magnitude of  $\kappa$  remains fixed but its phase varies periodically along the grating. In

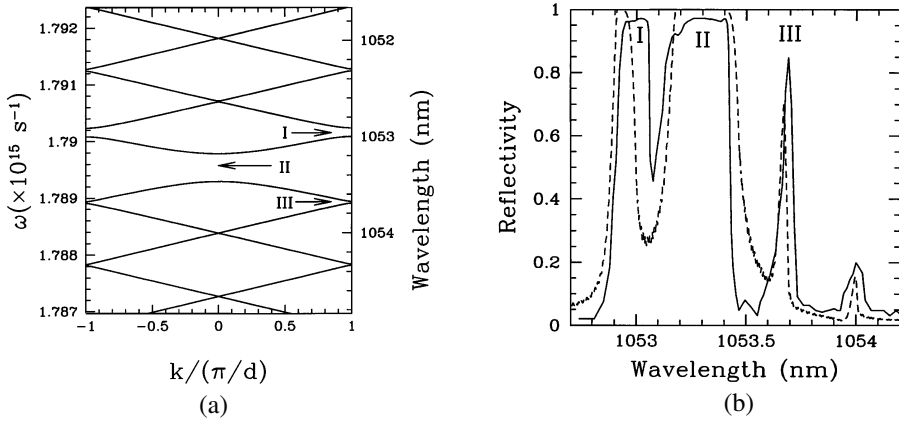


**Figure 1.27:** (a) Dispersion curves and (b) reflectivity spectrum for a 2.5-mm superstructure grating with  $d = 1$  mm. (From Ref. [178]; ©1996 OSA.)

all cases,  $\kappa(z)$  becomes a periodic function of  $z$ . It is this periodicity that modifies the stop band of a uniform grating. The period  $d$  of  $\kappa(z)$  is typically  $\sim 1$  mm. If the average index  $\bar{n}$  also changes with the same period  $d$ , both  $\delta$  and  $\kappa$  become periodic in the nonlinear coupled-mode equations.

The most striking feature of a superstructure grating is the appearance of additional photonic bandgaps on both branches of the dispersion curve seen in Figure 1.6 for a uniform grating. These bandgaps are referred to as *Rowland ghost gaps* [185]. Figure 1.27 shows the band structure of a 2.5-mm-long superstructure grating with  $d = 1$  mm together with the measured reflectivity spectrum. The Rowland ghost gaps labeled I and III occur on the opposite sides of the stop band and lead to two additional reflectivity peaks. Dispersive properties near these gaps are similar to those expected near the edges of the stop band II. As a result, nonlinear effects are quite similar. In particular, Bragg solitons can form on the branch where GVD is anomalous [176]. Indirect evidence of such solitons was seen in an experiment in which a 100-ps pulse was compressed to 38 ps within the 2.5-mm-long superstructure grating when it was tuned on the high-frequency side of the Rowland ghost gap I [178]. The pulse appeared to be evolving toward a Bragg soliton, which should form if the grating were long enough. Other nonlinear effects, such as optical bistability, modulation instability, and optical switching, should also occur near Rowland ghost gaps associated with a superstructure grating. In an interesting application, a superstructure grating was used to increase the repetition rate of a 3.4-ps pulse train from 10 to 40 GHz [181]. The grating was designed to have a band structure such that it reflected every fourth spectral peak of the input spectrum.

### 1.7.3 Transient and Dynamic Fiber Gratings

The fiber gratings discussed so far are of permanent nature in the sense that the periodic variations in the refractive index created during the manufacturing process may last

indefinitely under normal operating conditions. In contrast, a dynamic or transient grating is formed when the index changes are induced by pumping the fiber optically and last only as long as the pump light remains incident on the fiber. Such fiber gratings were first studied in 1992 and have remained an active topic of research since then [186]–[192].

It is easy to see how a dynamic grating can be formed through optical pumping. If a CW pump beam at the carrier frequency  $\omega_p$  is launched such that it propagates in the both forward and backward directions, it will form a standing wave whose intensity peaks periodically along the fiber length. The period of such a “fringe pattern” equals  $\Lambda_p = \pi/\beta_p = \lambda_p/(2\bar{n})$ , where  $\beta_p = \bar{n}(\omega_p)\omega_p/c$  is the propagation constant,  $\bar{n}(\omega_p)$  is the effective mode index, and  $\lambda_p$  is the pump wavelength. If such variations in the pump intensity change the material refractive index, a Bragg grating is formed. Indeed, the grating-formation technique discussed in Section 1.2.1 employs this approach to create permanent index changes.

If the fiber is doped with a rare-earth element such as erbium, the absorption or gain associated with dopants can be saturated by two counterpropagating pump beams, if their intensity is high enough to exceed the saturation intensity associated with the atomic transition. Through the Kramers–Kronig relation, such saturation helps to transfer periodic pump-intensity variations into period refractive-index variations along the fiber length, thereby creating a transient grating. In a 1992 experiment, a 12-m-long erbium-doped fiber, acting as an amplifier, was employed for this purpose [186]. The transient grating, created by launching  $<1$  mW of pump power, exhibited 75% reflectivity. Such a grating, once created, affects the pump beams through a nonlinear process known as *two-wave mixing* [187]. It can also be used for four-wave mixing by launching a third beam whose wavelength is close enough to the pump wavelength that it falls within the grating bandwidth.

In the case of an undoped silica fiber, the intensity-dependent term in Eq. (1.3.1), whose magnitude is governed by the nonlinear parameter  $n_2$ , can transfer the periodic pump-intensity variations into refractive-index variations along the fiber length. The required pump-intensity level exceeds  $10$  GW/cm<sup>2</sup> even for a relatively weak grating with index modulations  $\sim 10^{-5}$ . In spite of this requirement, such a technique was used in 2002 to realize modulation instability and to form gap solitons inside a dynamic fiber grating [190].

The basic idea consists of simultaneously launching three beams at frequencies  $\omega_0 - \Omega$ ,  $\omega_0$ , and  $\omega_0 + \Omega$  inside a birefringent fiber, making this scheme similar to that used for four-wave mixing. The two fields at frequencies  $\omega_0 \pm \Omega$ , copolarized along a principal axis of the fiber, propagate in the same direction and are launched with equal amplitudes, so that their combined intensity oscillates in the time domain at the frequency  $2\Omega$ . These periodic variations are seen by the third field, polarized orthogonal to the other two, because of an XPM-induced nonlinear coupling among the three waves. As a result, its propagation along the fiber is governed by [190]

$$\frac{\partial A}{\partial z} + \frac{i\beta_2}{2} \frac{\partial^2 A}{\partial t^2} = i\gamma|A|^2 A + 2i\kappa \cos(2\Omega t)A, \quad (1.7.4)$$

where  $\kappa = (4/3)\gamma P_g$  and  $P_g$  is the power launched into each of the two beams used

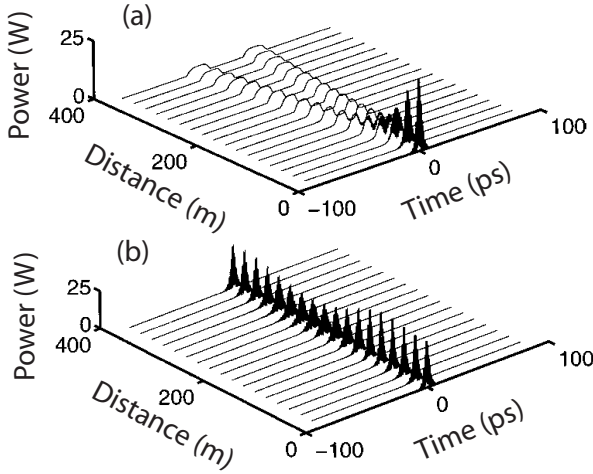


**Figure 1.28:** Evolution of two pulses of different wavelengths inside a fiber (a) without a grating ( $\kappa = 0$ ) and (b) with a dynamic grating ( $\kappa = 0.018 \text{ m}^{-1}$ ). Two pulses are trapped by the grating and form a gap soliton. (From Ref. [190]; ©2002 OSA.)

to create the grating. Since periodic index variations occur in time, such a grating is called *dynamic grating*.

Equation (1.7.4) can be solved by writing its solution in the form

$$A(z, t) = A_0(z, t) + A_1(z, t)e^{i(Kz - \Omega t)} + A_2(z, t)e^{i(Kz + \Omega t)}, \quad (1.7.5)$$

where  $A_1$  and  $A_2$  satisfy the following coupled-mode equations, if we assume that the amplitude of  $A_0$  is negligibly small [190]:

$$\frac{\partial A_1}{\partial z} + \Omega\beta_2 \frac{\partial A_1}{\partial t} + \frac{i\beta_2}{2} \frac{\partial^2 A_1}{\partial t^2} = i\kappa A_2 + i\gamma(|A_1|^2 + 2|A_2|^2)A_1, \quad (1.7.6)$$

$$\frac{\partial A_2}{\partial z} - \Omega\beta_2 \frac{\partial A_2}{\partial t} + \frac{i\beta_2}{2} \frac{\partial^2 A_2}{\partial t^2} = i\kappa A_1 + i\gamma(|A_2|^2 + 2|A_1|^2)A_2. \quad (1.7.7)$$

These equations have a form similar to Eqs. (1.3.11) and (1.3.12) with the major difference being that both  $A_1$  and  $A_2$  propagate in the forward direction. In this sense, they are closer to Eqs. (1.7.1) and (1.7.2), obtained earlier for long-period gratings.

Equations (1.7.6) and (1.7.7) exhibit all the features associated with traditional Bragg gratings [190]. In particular, such a dynamic grating exhibits modulation instability even in the normal-GVD regime of the fiber and supports Bragg solitons. If the second-order dispersion is neglected, Eqs. (1.7.6) and (1.7.7) are found to have the following solitary-wave solution:

$$A_1(z, t) = \sqrt{\frac{\kappa}{3\gamma}} \sin \psi \operatorname{sech} \left( \frac{\kappa \sin \psi}{\Omega\beta_2} t - \frac{i\psi}{2} \right) \exp(-i\kappa z \cos \psi), \quad (1.7.8)$$

$$A_2(z, t) = -\sqrt{\frac{\kappa}{3\gamma}} \sin \psi \operatorname{sech} \left( \frac{\kappa \sin \psi}{\Omega\beta_2} t + \frac{i\psi}{2} \right) \exp(-i\kappa z \cos \psi), \quad (1.7.9)$$

where  $\psi$  can have any value in the range  $0 \leq \psi \leq \pi$ . This free parameter determines both the amplitude and width of a family of the Bragg solitons in Eqs. (1.7.8) and (1.7.9). In fact, these solitons correspond to the gap solitons discussed earlier in Section 1.6, because they are stationary in the local reference frame of a moving dynamic grating.

Physically, each such gap soliton represents a superposition of two pulses of different frequencies ( $\omega_0 \pm \Omega$ ) that travel at different speeds in the absence of the grating. Indeed, numerical solutions of Eqs. (1.7.6) and (1.7.7) with  $\kappa = 0$  show that the two pulses separate rapidly [190]. Figure 1.28(a) shows this behavior for a 400-m-long fiber using  $\Omega/2\pi = 0.5$  THz and  $\psi = \pi/2$ . When a dynamic grating is present, the two pulses form a gap soliton that is trapped by the grating and appears stationary in the frame of the input pulse. Figure 1.28(b) shows such trapping by changing  $\kappa$  from 0 to  $0.018 \text{ m}^{-1}$ , while keeping all other parameters the same. A similar effect was predicted as early as 1989, and the resulting solitary waves were called *resonance solitons* [193]. The trapping mechanism is similar to that discussed in Section 6.5 of Ref. [2] in the context of vector solitons forming in a birefringent fiber.

## Problems

- 1.1 Derive Eq. (1.1.1) from the phase-matching condition in Eq. (1.1.2).
- 1.2 Use Eq. (1.1.1) to find the grating period  $\Lambda$  for a fiber Bragg grating reflecting light near  $1.55 \mu\text{m}$ . Assume  $m = 1$  and  $\bar{n} = 1.45$ .
- 1.3 Describe the mechanism through which absorption of ultraviolet light produces changes in the refractive index of silica fibers.
- 1.4 Discuss the holographic and phase-mask techniques used to make fiber gratings. Sketch the experimental setup in each case.
- 1.5 Derive the nonlinear coupled-mode equations, (1.3.11) and (1.3.12), for fiber gratings starting from the Helmholtz equation (1.3.2).
- 1.6 What is meant by the stop band of a grating? Starting from the linear coupled-mode equations, (1.3.13) and (1.3.14), find the dispersion relation and the width of the stop band.
- 1.7 An optical pulse is transmitted through a fiber grating with its spectrum located close to but outside the stop band. Its energy is small enough that nonlinear effects are negligible. Derive an expression for the group velocity of the pulse.
- 1.8 For the previous problem, derive expressions for the second- and third-order dispersion induced by the grating. You can neglect the material and waveguide dispersion of silica fibers.
- 1.9 Derive an expression for the reflectivity of a fiber grating by solving the coupled-mode equations, (1.3.13) and (1.3.14). Plot it as a function of  $\delta/\kappa$  using  $\kappa L = 3$ .
- 1.10 The coupling coefficient of an apodized grating of length  $L$  varies as  $\kappa(z) = \kappa_0 \exp[-(4 - 8z/L)^{2m}]$ . Solve the linear coupled-mode equations, (1.3.13) and

(1.3.14), numerically and plot the reflectivity spectrum for  $m = 1, 2, 3$  as a function of  $\delta/\kappa$  using  $\kappa L = 3$ .

- 1.11** Solve the nonlinear coupled-mode equations, (1.4.1) and (1.4.2), assuming that the powers of the forward- and backward-propagating waves are constant in time and along the grating length. Find the relative power levels when  $\delta/\kappa = 1.05$  and  $\gamma P_0/\kappa = 2$ , where  $P_0$  is the total power.
- 1.12** Use the CW solution obtained in the previous problem to discuss how the stop band of a fiber grating is affected at high power levels because of the nonlinear effects.
- 1.13** Perturb the CW solution of Eqs. (1.4.1) and (1.4.2) and discuss the conditions under which it may become unstable.
- 1.14** Develop a computer program for solving Eqs. (1.4.1) and (1.4.2) numerically and use it to reproduce the results shown in Figure 1.18.

## References

- [1] M. Born and E. Wolf, *Principles of Optics*, 7th ed. (Cambridge University Press, New York, 1999), Section 8.6.
- [2] G. P. Agrawal, *Nonlinear Fiber Optics*, 4th ed. (Academic Press, Boston, 2007).
- [3] K. O. Hill, Y. Fujii, D. C. Johnson, and B. S. Kawasaki, *Appl. Phys. Lett.* **32**, 647 (1978).
- [4] B. S. Kawasaki, K. O. Hill, D. C. Johnson, and Y. Fujii, *Opt. Lett.* **3**, 66 (1978).
- [5] J. Bures, J. Lapierre, and D. Pascale, *Appl. Phys. Lett.* **37**, 860 (1980).
- [6] J. Lapierre, J. Bures, and D. Pascale, *Opt. Commun.* **40**, 95 (1981).
- [7] D. K. W. Lam and B. K. Garside, *Appl. Opt.* **20**, 440 (1982).
- [8] J. Lapierre, J. Bures, and G. Chevalier, *Opt. Lett.* **7**, 37 (1982).
- [9] J. Bures, S. Lacroix, and J. Lapierre, *Appl. Opt.* **21**, 3502 (1982).
- [10] D. K. W. Lam, B. K. Garside, and K. O. Hill, *Opt. Lett.* **7**, 291 (1982).
- [11] M. Parent, J. Bures, S. Lacroix, and J. Lapierre, *Appl. Opt.* **24**, 354 (1985).
- [12] J. Stone, *J. Appl. Phys.* **62**, 4371 (1987).
- [13] C. P. Kuo, U. Österberg, C. T. Seaton, G. I. Stegeman, and K. O. Hill, *Opt. Lett.* **13**, 1032 (1988).
- [14] F. P. Payne, *Electron. Lett.* **25**, 498 (1989).
- [15] H. G. Park and B. Y. Park, *Electron. Lett.* **25**, 737 (1989).
- [16] F. Ouellette, *Electron. Lett.* **25**, 1590 (1989).
- [17] G. Meltz, W. W. Morey, and W. H. Glen, *Opt. Lett.* **14**, 823 (1989).
- [18] R. Kashyap, J. R. Armitage, R. Wyatt, S. T. Davey, and D. L. Williams, *Electron. Lett.* **26**, 730 (1990).
- [19] K. O. Hill, B. Malo, K. A. Vineberg, F. Bilodeau, D. C. Johnson, and I. Skinner, *Electron. Lett.* **26**, 1270 (1990).
- [20] S. La Rochelle, V. Mizrahi, G. I. Stegeman, and J. Sipe, *Appl. Phys. Lett.* **57**, 747 (1990).
- [21] S. La Rochelle, Y. Hibino, V. Mizrahi, and G. I. Stegeman, *Electron. Lett.* **26**, 1459 (1990).
- [22] J. P. Bernardin and N. M. Lawandy, *Opt. Commun.* **79**, 194 (1990).
- [23] D. P. Hand and P. St. J. Russell, *Opt. Lett.* **15**, 104 (1990).

- [24] B. Malo, K. A. Vineberg, F. Bilodeau, J. Albert, D. C. Johnson, and K. O. Hill, *Opt. Lett.* **15**, 953 (1990).
- [25] G. A. Ball, W. W. Morey, and J. P. Waters, *Electron. Lett.* **26**, 1829 (1990).
- [26] V. Mizrahi, S. La Rochelle, and G. I. Stegeman, *Phys. Rev. A* **43**, 433 (1991).
- [27] S. E. Kanellopoulos, V. A. Handerek, H. Jamshidi, and A. J. Rogers, *IEEE Photon. Technol. Lett.* **3**, 244 (1991).
- [28] S. Legoubin, E. Fertein, M. Douay, P. Bernage, P. Nidy, F. Bayon, and T. Georges, *Electron. Lett.* **27**, 1945 (1991).
- [29] P. St. J. Russell, L. J. Poyntz-Wright, and D. P. Hand, *Proc. SPIE* **1373**, 126 (1991).
- [30] G. Meltz and W. W. Morey, *Proc. SPIE* **1516**, 185 (1991).
- [31] T. E. Tsai, C. G. Askins, and E. J. Friebele, *Appl. Phys. Lett.* **61**, 390 (1992).
- [32] C. G. Askins, T. E. Tsai, G. M. Williams, M. A. Puttnam, M. Bashkansky, and E. J. Friebele, *Opt. Lett.* **17**, 833 (1992).
- [33] H. G. Limberger, P. Y. Fonjallaz, and R. P. Salathé, *Electron. Lett.* **29**, 47 (1993).
- [34] J. L. Archambault, L. Reekie, and P. St. J. Russell, *Electron. Lett.* **29**, 28 (1993); *Electron. Lett.* **29**, 453 (1993).
- [35] L. Long, J. L. Archambault, L. Reekie, P. St. J. Russell, and D. N. Payne, *Opt. Lett.* **18**, 861 (1993).
- [36] K. O. Hill, B. Malo, F. Bilodeau, D. C. Johnson, and J. Albert, *Appl. Phys. Lett.* **62**, 1035 (1993).
- [37] D. Z. Anderson, V. Mizrahi, T. Erdogan, and A. E. White, *Electron. Lett.* **29**, 566 (1993).
- [38] B. Malo, D. C. Johnson, F. Bilodeau, J. Albert, and K. O. Hill, *Opt. Lett.* **18**, 1277 (1993).
- [39] P. J. Lemaire, R. M. Atkins, V. Mizrahi, and W. A. Reed, *Electron. Lett.* **29**, 1191 (1993).
- [40] L. Long, J. L. Archambault, L. Reekie, P. St. J. Russell, and D. N. Payne, *Electron. Lett.* **29**, 1577 (1993).
- [41] J. D. Prohaska, E. Snitzer, S. Rishton, and V. Boegli, *Electron. Lett.* **29**, 1614 (1993).
- [42] K. C. Byron, K. Sugden, T. Bricheno, and I. Bennion, *Electron. Lett.* **29**, 1659 (1993).
- [43] B. Malo, K. O. Hill, F. Bilodeau, D. C. Johnson, and J. Albert, *Appl. Phys. Lett.* **62**, 1668 (1993).
- [44] H. Patrick and S. L. Gilbert, *Opt. Lett.* **18**, 1484 (1993).
- [45] K. O. Hill, B. Malo, F. Bilodeau, and D. C. Johnson, *Annu. Rev. Mater. Sci.* **23**, 125 (1993).
- [46] S. J. Mihailor and M. C. Gower, *Electron. Lett.* **30**, 707 (1994).
- [47] M. C. Farries, K. Sugden, D. C. J. Reid, I. Bennion, A. Molony, and M. J. Goodwin, *Electron. Lett.* **30**, 891 (1994).
- [48] R. Kashyap, *Fiber Bragg Gratings* (Academic Press, Boston, 1999).
- [49] A. Othonos and K. Kalli, *Fiber Bragg Gratings: Fundamentals and Applications in Telecommunications and Sensing* (Artech House, Boston, 1999).
- [50] M. N. Zervas, *Fiber Bragg Gratings for Optical Fiber Communications* (Wiley, Hoboken, NJ, 2001).
- [51] P. N. Butcher and D. Cotter, *Elements of Nonlinear Optics* (Cambridge University Press, Cambridge, UK, 1990), p. 315.
- [52] T. Erdogan, V. Mizrahi, P. J. Lemaire, and D. Monroe, *J. Appl. Phys.* **76**, 73 (1994).
- [53] H. Patrick, S. L. Gilbert, A. Lidgard, and M. D. Gallagher, *J. Appl. Phys.* **78**, 2940 (1995).
- [54] S. R. Baker, H. N. Rourke, V. Baker, and D. Goodchild, *J. Lightwave Technol.* **15**, 1470 (1997).

- [55] S. Kannan, J. Z. Y. Gus, and P. J. Lemaire, *J. Lightwave Technol.* **15**, 1478 (1997).
- [56] N. K. Viswanathan and D. L. LaBrake, *J. Lightwave Technol.* **22**, 1990 (2004).
- [57] J. Canning, *Opt. Fiber Technol.* **6**, 275 (2000).
- [58] A. Canagasabay, J. Canning, and N. Groothoff, *Opt. Lett.* **28**, 1108 (2003).
- [59] K. P. Chen, P. R. Herman, and R. Tam, *J. Lightwave Technol.* **21**, 1958 (2003).
- [60] M. Fokine and W. Margulis, *Opt. Lett.* **25**, 30 (2000).
- [61] M. Lancry, P. Niay, M. Douay, C. Depecker, P. Cordier, and B. Poumellec, *J. Lightwave Technol.* **24**, 1376 (2006).
- [62] R. Kashyap, H.-G. Froehlich, A. Swanton, and D. J. Armes, *Electron. Lett.* **32**, 1807 (1996).
- [63] J. Albert, S. Theriault, F. Bilodeau, D. C. Johnson, K. O. Hill, P. Sixt, and M. J. Rooks, *IEEE Photon. Technol. Lett.* **8**, 1334 (1996).
- [64] P. St. J. Russell and D. P. Hand, *Electron. Lett.* **26**, 1840 (1990).
- [65] D. C. Johnson, F. Bilodeau, B. Malo, K. O. Hill, P. G. J. Wigley, and G. I. Stegeman, *Opt. Lett.* **17**, 1635 (1992).
- [66] A. M. Vangsarkar, P. J. Lemaire, J. B. Judkins, V. Bhatia, T. Erdogan, and J. Sipe, *J. Lightwave Technol.* **14**, 58 (1996).
- [67] K. M. Davis, K. Miura, N. Sugimoto, and K. Hirao, *Opt. Lett.* **21**, 1729 (1996).
- [68] C. B. Schaffer, A. Brodeur, J. F. Garca, and E. Mazur, *Opt. Lett.* **26**, 93 (2001).
- [69] M. Will, S. Nolte, B. N. Chichkov, and A. Tünnermann, *Appl. Opt.* **41**, 4360 (2002).
- [70] A. M. Streltsov and N. F. Borrelli, *J. Opt. Soc. Am. B* **19**, 2496 (2002).
- [71] A. Saliminia, N. T. Nguyen, M. C. Nadeau, S. Petit, S. L. Chin, and R. Vallée, *J. Appl. Phys.* **93**, 3724 (2003).
- [72] H. Zhang, S. M. Eaton, and P. R. Herman, *Opt. Express* **14**, 4826 (2006).
- [73] Y. Kondo, K. Nouchi, T. Mitsuyuy, M. Watanabe, P. G. Kanansky, and K. Hirao, *Opt. Lett.* **24**, 646 (1999).
- [74] S. J. Mihailov, C. W. Smelser, D. Grobnic, R. B. Walker, P. Lu, H. Ding, and J. Unruh, *J. Lightwave Technol.* **22**, 94-100 (2004).
- [75] C. W. Smelser, S. J. Mihailov, and D. Grobnic, *Opt. Express* **13**, 5377 (2005).
- [76] L. Sudrie, M. Franco, B. Prade, and A. Mysyrowicz, *Opt. Commun.* **191**, 333 (2001).
- [77] A. Dragomir, D. N. Nikogosyan, K. A. Zagorulko, P. G. Kryukov, and E. M. Dianov, *Opt. Lett.* **28**, 2171 (2003).
- [78] K. A. Zagorulko, P. G. Kryukov, Yu. V. Larionov, A. A. Rybaltovskiy, E. M. Dianov, S. V. Chekalin, Yu. A. Matveets, and V. O. Kompanets, *Opt. Express* **12**, 5996 (2004).
- [79] S. A. Slattery, D. N. Nikogosyan, and G. Brambilla, *J. Opt. Soc. Am. B* **22**, 354 (2005).
- [80] P. St. J. Russell, *J. Mod. Opt.* **38**, 1599 (1991).
- [81] H. A. Haus, *Waves and Fields in Optoelectronics* (Prentice-Hall, Englewood Cliffs, NJ, 1984).
- [82] D. Marcuse, *Theory of Dielectric Optical Waveguides* (Academic Press, San Diego, CA, 1991).
- [83] A. Yariv, *Optical Electronics in Modern Communications*, 5th ed. (Oxford University Press, New York, 1997).
- [84] G. P. Agrawal and N. K. Dutta, *Semiconductor Lasers*, 2nd ed. (Van Nostrand Reinhold, New York, 1993).
- [85] B. Crosignani, A. Cutolo, and P. Di Porto, *J. Opt. Soc. Am. B* **72**, 515 (1982).
- [86] N. M. Litchinitser, B. J. Eggleton, and D. B. Patterson, *J. Lightwave Technol.* **15**, 1303 (1997).

- [87] G. P. Agrawal, *Lightwave Technology: Telecommunication Systems* (Wiley, Hoboken, NJ, 2005).
- [88] B. J. Eggleton, C. M. de Sterke, and R. E. Slusher, *J. Opt. Soc. Am. B* **16**, 587 (1999).
- [89] H. G. Winful, J. H. Marburger, and E. Garmire, *Appl. Phys. Lett.* **35**, 379 (1979).
- [90] H. G. Winful and G. D. Cooperman, *Appl. Phys. Lett.* **40**, 298 (1982).
- [91] H. G. Winful, *Appl. Phys. Lett.* **46**, 527 (1985).
- [92] W. Chen and D. L. Mills, *Phys. Rev. Lett.* **58**, 160 (1987); *Phys. Rev. B* **36**, 6269 (1987).
- [93] D. L. Mills and S. E. Trullinger, *Phys. Rev. B* **36**, 947 (1987).
- [94] C. M. de Sterke and J. E. Sipe, *Phys. Rev. A* **38**, 5149 (1988); *Phys. Rev. A* **39**, 5163 (1989).
- [95] C. M. de Sterke and J. E. Sipe, *J. Opt. Soc. Am. B* **6**, 1722 (1989).
- [96] S. Larochelle, V. Mizrahi, and G. Stegeman, *Electron. Lett.* **26**, 1459 (1990).
- [97] C. M. de Sterke and J. E. Sipe, *Phys. Rev. A* **43**, 2467 (1991).
- [98] N. D. Sankey, D. F. Prelewitz, and T. G. Brown, *Appl. Phys. Lett.* **60**, 1427 (1992); *J. Appl. Phys.* **73**, 1 (1993).
- [99] J. Feng, *Opt. Lett.* **18**, 1302 (1993).
- [100] Y. S. Kivshar, *Phys. Rev. Lett.* **70**, 3055 (1993).
- [101] C. M. de Sterke and J. E. Sipe, in *Progress in Optics*, Vol. 33, E. Wolf, Ed. (Elsevier, Amsterdam, 1994), Chap. 3.
- [102] P. St. J. Russell and J. L. Archambault, *J. Phys. III France* **4**, 2471 (1994).
- [103] M. Scalora, J. P. Dowling, C. M. Bowden, and M. J. Bloemer, *Opt. Lett.* **19**, 1789 (1994).
- [104] S. Radic, N. George, and G. P. Agrawal, *Opt. Lett.* **19**, 1789 (1994); *J. Opt. Soc. Am. B* **12**, 671 (1995).
- [105] S. Radic, N. George, and G. P. Agrawal, *IEEE J. Quantum Electron.* **31**, 1326 (1995).
- [106] A. R. Champneys, B. A. Malomed, and M. J. Friedman, *Phys. Rev. Lett.* **80**, 4169 (1998).
- [107] A. E. Kozhokin, G. Kurizki, and B. Malomed, *Phys. Rev. Lett.* **81**, 3647 (1998).
- [108] C. Conti, G. Asanto, and S. Trillo, *Opt. Express* **3**, 389 (1998).
- [109] Y. A. Logvin and V. M. Volkov, *J. Opt. Soc. Am. B* **16**, 774 (1999).
- [110] H. M. Gibbs, *Optical Bistability: Controlling Light with Light* (Academic Press, San Diego, CA, 1985).
- [111] G. P. Agrawal and S. Radic, *IEEE Photon. Technol. Lett.* **6**, 995 (1994).
- [112] C. M. de Sterke and J. E. Sipe, *Phys. Rev. A* **42**, 2858 (1990).
- [113] H. G. Winful, R. Zamir, and S. Feldman, *Appl. Phys. Lett.* **58**, 1001 (1991).
- [114] A. B. Aceves, C. De Angelis, and S. Wabnitz, *Opt. Lett.* **17**, 1566 (1992).
- [115] C. M. de Sterke, *Phys. Rev. A* **45**, 8252 (1992).
- [116] B. J. Eggleton, C. M. de Sterke, R. E. Slusher, and J. E. Sipe, *Electron. Lett.* **32**, 2341 (1996).
- [117] C. M. de Sterke, *J. Opt. Soc. Am. B* **15**, 2660 (1998).
- [118] K. Porsezian, K. Senthilnathan, and S. Devipriya, *IEEE J. Quantum Electron.* **41**, 789 (2005).
- [119] J. E. Sipe and H. G. Winful, *Opt. Lett.* **13**, 132 (1988).
- [120] C. M. de Sterke and J. E. Sipe, *Phys. Rev. A* **42**, 550 (1990).
- [121] C. M. de Sterke, D. G. Salinas, and J. E. Sipe, *Phys. Rev. E* **54**, 1969 (1996).
- [122] T. Iizuka and M. Wadati, *J. Opt. Soc. Am. B* **14**, 2308 (1997).
- [123] C. M. de Sterke and B. J. Eggleton, *Phys. Rev. E* **59**, 1267 (1999).

- [124] B. J. Eggleton, C. M. de Sterke, A. B. Aceves, J. E. Sipe, T. A. Strasser, and R. E. Slusher, *Opt. Commun.* **149**, 267 (1998).
- [125] D. N. Christodoulides and R. I. Joseph, *Phys. Rev. Lett.* **62**, 1746 (1989).
- [126] A. B. Aceves and S. Wabnitz, *Phys. Lett. A* **141**, 37 (1989).
- [127] J. Feng and F. K. Kneubühl, *IEEE J. Quantum Electron.* **29**, 590 (1993).
- [128] B. J. Eggleton, R. R. Slusher, C. M. de Sterke, P. A. Krug, and J. E. Sipe, *Phys. Rev. Lett.* **76**, 1627 (1996).
- [129] C. M. de Sterke, N. G. R. Broderick, B. J. Eggleton, and M. J. Steel, *Opt. Fiber Technol.* **2**, 253 (1996).
- [130] B. J. Eggleton, C. M. de Sterke, and R. E. Slusher, *J. Opt. Soc. Am. B* **14**, 2980 (1997).
- [131] D. Taverner, N. G. R. Broderick, D. J. Richardson, M. Isben, and R. I. Laming, *Opt. Lett.* **23**, 259 (1998).
- [132] D. Taverner, N. G. R. Broderick, D. J. Richardson, R. I. Laming, and M. Isben, *Opt. Lett.* **23**, 328 (1998).
- [133] C. M. de Sterke, *Opt. Express* **3**, 405 (1998).
- [134] N. G. R. Broderick, D. Taverner, and D. J. Richardson, *Opt. Express* **3**, 447 (1998).
- [135] B. J. Eggleton, G. Lenz, R. E. Slusher, and N. M. Litchinitser, *Appl. Opt.* **37**, 7055 (1998).
- [136] N. M. Litchinitser, B. J. Eggleton, C. M. de Sterke, A. B. Aceves, and G. P. Agrawal, *J. Opt. Soc. Am. B* **16**, 18 (1999).
- [137] N. G. R. Broderick, D. J. Richardson, and M. Isben, *Opt. Lett.* **25**, 536 (2000).
- [138] V. Perlin and H. G. Winful, *Phys. Rev. A* **64**, 043804 (2001).
- [139] H. Lee and G. P. Agrawal, *IEEE J. Quantum Electron.* **39**, 508 (2003).
- [140] K. Senthilnathan, K. Porsezian, P. Ramesh Babu, and V. Santhanam, *IEEE J. Quantum Electron.* **39**, 1492 (2003).
- [141] J. T. Mok, I. C. M. Littler, E. Tsoy, and B. J. Eggleton, *Opt. Lett.* **30**, 2457 (2005).
- [142] A. Rosenthal and M. Horowitz, *Opt. Lett.* **31**, 1334 (2006).
- [143] M. Asobe, *Opt. Fiber Technol.* **3**, 142 (1997).
- [144] W. E. Thirring, *Ann. Phys. (NY)* **3**, 91 (1958).
- [145] A. V. Mikhailov, *JETP Lett.* **23**, 320 (1976).
- [146] E. A. Kuznetsov and A. V. Mikhailov, *Teor. Mat. Fiz.* **30**, 193 (1977).
- [147] D. J. Kaup and A. C. Newell, *Lett. Nuovo Cimento* **20**, 325 (1977).
- [148] D. David, J. Harnad, and S. Shnider, *Lett. Math. Phys.* **8**, 27 (1984).
- [149] H. Kawaguchi, K. Inoue, T. Matsuoka, and K. Otsuka, *IEEE J. Quantum Electron.* **21**, 1314 (1985).
- [150] M. J. Adams and R. Wyatt, *IEE Proc.* **134** 35 (1987).
- [151] M. J. Adams, *Opt. Quantum Electron.* **19**, S37 (1987).
- [152] C. M. de Sterke, *Opt. Lett.* **17**, 914 (1992).
- [153] N. G. R. Broderick, D. Taverner, D. J. Richardson, M. Isben, and R. I. Laming, *Phys. Rev. Lett.* **79**, 4566 (1997); *Opt. Lett.* **22**, 1837 (1997).
- [154] A. Melloni, M. Chinello, and M. Martinelli, *IEEE Photon. Technol. Lett.* **12**, 42 (2000).
- [155] S. Lee and S. T. Ho, *Opt. Lett.* **18**, 962 (1993).
- [156] W. Samir, S. J. Garth, and C. Pask, *J. Opt. Soc. Am. B* **11**, 64 (1994).
- [157] W. Samir, C. Pask, and S. J. Garth, *Opt. Lett.* **19**, 338 (1994).
- [158] S. Pereira and J. E. Sipe, *Opt. Express* **3**, 418 (1998).
- [159] R. E. Slusher, S. Spälter, B. J. Eggleton, S. Pereira, and J. E. Sipe, *Opt. Lett.* **25**, 749 (2000).

- [160] S. Broderick, *Opt. Commun.* **148**, 90 (1999).
- [161] K. O. Hill, B. Malo, K. A. Vineberg, F. Bilodeau, D. C. Johnson, and I. Skinner, *Electron. Lett.* **26**, 1270 (1990).
- [162] B. J. Eggleton, R. E. Slusher, J. B. Judkins, J. B. Stark, and A. M. Vengsarkar, *Opt. Lett.* **22**, 883 (1997).
- [163] J. N. Kutz, B. J. Eggleton, J. B. Stark, and R. E. Slusher, *IEEE J. Sel. Topics Quantum Electron.* **3**, 1232 (1997).
- [164] Y. Jeong and B. Lee, *IEEE J. Quantum Electron.* **35**, 1284 (1999).
- [165] V. E. Perlin and H. G. Winful, *J. Lightwave Technol.* **18**, 329, (2000).
- [166] G. W. Chern, J. F. Chang, and L. A. Wang, *J. Opt. Soc. Am. B* **19**, 1497, (2002).
- [167] D. Pudo, E. C. Mägi, and B. J. Eggleton, *Opt. Express* **14**, 3763 (2006).
- [168] J. A. R Williams, I. Bennion, and L. Zhang, *IEEE Photon. Technol. Lett.* **7**, 491 (1995).
- [169] A. Galvanauskas, P. A. Krug, and D. Harter, *Opt. Lett.* **21**, 1049 (1996).
- [170] G. Lenz, B. J. Eggleton, and N. M. Litchinitser, *J. Opt. Soc. Am. B* **15**, 715 (1998).
- [171] R. E. Slusher, B. J. Eggleton, T. A. Strasser, and C. M. de Sterke, *Opt. Express* **3**, 465 (1998).
- [172] N. M. Litchinitser, G. P. Agrawal, B. J. Eggleton, and G. Lenz, *Opt. Express* **3**, 411 (1998).
- [173] C. S. Yang, Y. C. Chiang, and H. C. Chang, *IEEE J. Quantum Electron.* **40**, 1337 (2004).
- [174] V. Jayaraman, D. Cohen, and L. Coldren, *Appl. Phys. Lett.* **60**, 2321 (1992).
- [175] B. J. Eggleton, P. A. Krug, L. Poladian, and F. Ouellette, *Electron. Lett.* **30**, 1620 (1994).
- [176] N. G. R. Broderick, C. M. de Sterke, and B. J. Eggleton, *Phys. Rev. E* **52**, R5788 (1995).
- [177] C. M. de Sterke and N. G. R. Broderick, *Opt. Lett.* **20**, 2039 (1995).
- [178] B. J. Eggleton, C. M. de Sterke, and R. E. Slusher, *Opt. Lett.* **21**, 1223 (1996).
- [179] N. G. R. Broderick and C. M. de Sterke, *Phys. Rev. E* **55**, 3232 (1997).
- [180] C. M. de Sterke, B. J. Eggleton, and P. A. Krug, *J. Lightwave Technol.* **15**, 1494 (1997).
- [181] P. Petropoulos, M. Isben, M. N. Zervas, and D. J. Richardson, *Opt. Lett.* **25**, 521 (2000).
- [182] H. Li, Y. Sheng, Y. Li, and J. E. Rothenberg, *J. Lightwave Technol.* **21**, 2074 (2003).
- [183] H. Lee and G. P. Agrawal, *IEEE Photon. Technol. Lett.* **15**, 1091 (2003); *IEEE Photon. Technol. Lett.* **16**, 635 (2004).
- [184] J. E. Rothenberg, H. Li, Y. Sheng, J. Popelek, and J. Zweiback, *Opt. Lett.* **31**, 1199 (2006).
- [185] P. St. J. Russell, *Phys. Rev. Lett.* **56**, 596 (1986).
- [186] S. Frisken, *Opt. Lett.* **17**, 1776 (1992).
- [187] B. Fischer, J. L. Zyskind, J. W. Sulhoff, and D. J. DiGiovanni, *Opt. Lett.* **18**, 2108 (1993).
- [188] M. D. Feuer, *IEEE Photon. Technol. Lett.* **10**, 1587 (1998).
- [189] S. A. Havstad, B. Fischer, A. E. Willner, and M. G. Wickham, *Opt. Lett.* **24**, 1466 (1999).
- [190] S. Pitois, M. Haelterman, and G. Millot, *J. Opt. Soc. Am. B* **19**, 782 (2002).
- [191] S. Stepanov, E. Hernández, and M. Plata, *Opt. Lett.* **29**, 1327 (2004); *J. Opt. Soc. Am. B* **22**, 1161 (2005).
- [192] X. Fan, Z. He, Y. Mizuno, and K. Hotate, *Opt. Express* **13**, 5756 (2005).
- [193] S. Wabnitz, *Opt. Lett.* **14**, 1071 (1989).